Molecular Simulations: Probing Systems from the Nanoscale to Mesoscale

K. G. Ayappa, Ateeque Malani, Patil Kalyan AND Foram Thakkar

Abstract | The review is concerned with the role that molecular simulations have played in enhancing our understanding of systems ranging from the nanoscale to mesoscale. The structure and dynamics of nanoscopically confined films, fluids confined in carbon nanotubes, self assembled monolayers and mesoscale simulations of a variety of complex fluid systems using dissipative particle dynamics, are covered in this review. Molecular simulations have significantly enhanced our understanding of confined fluid behaviour and self assembled monolayers, aiding in the interpretation of experimental findings on these systems. The science of these systems influences our evaluation of interfacial processes such as freezing, adsorption, wetting, adhesion, friction and lubrication, impacting a wide range of technologies ranging from fluid separations, sensors, microelectromechanical (MEMS) devices to nanofluidic systems. The last part of the review concerns the study of mesoscale systems, where length and time scales of the processes are typically greater than those sampled in conventional molecular simulations (1–10 nm, 1–10 ns). The emphasis is on a relatively new technique called dissipative particle dynamics and its potential in studying complex fluid phenomenon, from self assembly in oil–water–surfactant mixtures, polymer structure and rheology to continuum fluid mechanics.

Department of Chemical Engineering, Indian Institute of Science, Bangalore, India 560012

Keywords: Molecular Simulations, Nanofluids, Self Assembled, Monolayers Carbon Nanotubes, Dissipative Particle Dynamics

1. Introduction

Molecular simulations has become an indispensable tool in developing our understanding of various systems ranging from simple monoatomic fluids to complex fluids made up of polymers, surfactants and proteins. From the early Monte Carlo[1] and molecular dynamics[2] (MD) simulations of hard sphere systems and later on soft sphere fluids,[3,4] simulation techniques have advanced significantly, and today a variety of methods are available for evaluating thermodynamic, structural and dynamical properties. A number of standard textbooks cover this vast subject.[5–9] Technical advances in manipulating systems at the nanoscale opens up possibilities for creating new devices with a wide range of technological and scientific implication. This review is concerned with the role that molecular simulations have played in enhancing our understanding of the interplay between interactions at the atomic scale and system properties of a few technologically important nanoscale processes.

Figure 1 illustrates the regime of length and time scales probed using classical molecular dynamics simulations. In this regime, where the length scales range from 1–10 nm (10^{-9}m) and time scales are typically in the ns (10^{-9}s) regime, we will review the literature concerned with molecularly confined fluid films and fluids confined in carbon nanotubes. When fluids are confined to length scales on the

order of a few atomic diameters, the structure and dynamics are considerably altered. Molecular simulations have proved to be a versatile tool in providing an atomic perspective on the behaviour of fluids in nanopores, and has advanced our understanding of the interaction of fluids confined in a variety of situations. Confined fluids occur in technologies such as catalysis, gas adsorption, gas separation, boundary lubrication, adhesion and oil recovery. The study of confined fluids is expected to be important in understanding newer technologies based on microelectromechanical systems (MEMS) where issues such as adhesion and friction are critical; in the search for efficient storage materials for natural gas and hydrogen; and microfluidics where interfacial effects are expected to influence mixing and stability of flows. The structure and dynamics of inhomogeneous fluids in slit-shaped pores will be reviewed in Section 2 and fluids confined in carbon nanotubes will be discussed in Section 3.

The second system which falls within the purview of length and time scales of classical molecular dynamics simulations, is the structure and dynamics of self assembled monolayers where long chain alkane molecules organize into ordered two dimensional structures on a solid surface. The formation of self assembled structures opens up the possibility of modifying surface properties and has implications in friction, wear, wetting, adsorption, sensors and lubricating contacts. Section 4 of the review is devoted to discussing the equilibrium properties of self assembled monolayers as well as the literature devoted to analyzing their adhesion and friction properties.

The last part of the review (Section 5) is concerned with the regime denoted as mesoscale in Figure 1. In this regime one is interested in probing systems on the time scale of a few μs and length scales of 10–1000 nm. These systems include the structure and dynamics of phases with complex microstructure that form in oil–water–surfactant systems and dynamics of colloidal suspensions. These systems are important in detergency, wetting and biological processes at the level of the cell membrane. Several coarse grained methods are used to study system properties at the mesoscale. Coarse grained molecular dynamics, Brownian dynamics, dissipative particle dynamics and lattice Boltzmann methods are a few of the currently used methods. In this review we restrict our attention to a relatively recent mesoscale technique called dissipative particle dynamics. The method is applicable across both the mesoscale and continuum regimes (see Figure 1).

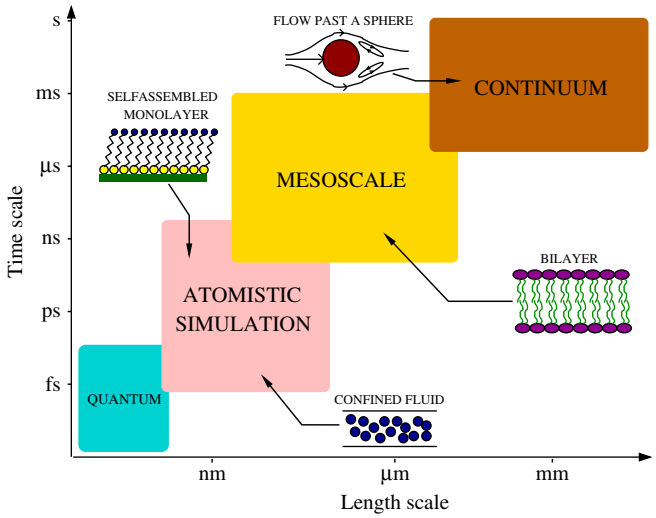

Figure 1: Schematic representation of various simulation methods and the corresponding length and time scales typically accessible to each method. Confined fluids, self assembled monolayers, the bilayer phase and flow past a sphere are representative of the systems discussed in this review. Quantum methods include density functional, ab inito and Carr-Parinello molecular dynamics. Atomisitic methods include molecular dynamics and Monte Carlo simulations. Mesoscale methods include coarse grained molecular dynamics, dissipative particle dynamics, Brownian dynamics and Lattice Boltzmann simulations. Continuum methods involve solution of heat, mass and momentum transport equations using a variety of numerical methods such as finite element and finite difference methods. Methods such as coarse grained molecular dynamics include the overlap region between atomistic and mesoscale simulations, while dissipative particle dynamics and Lattice Boltzmann methods include the overlap between mescoscale and continuum regimes.

2. Fluids Confined in Slit Pores

The slit pore is a versatile prototype for studying effects of atomic scale confinement on the induced density inhomogeneities, thermodynamics and transport of confined fluids. The slit pore commonly used in simulations is infinite in two directions and is made up of finite width, H, as shown in Figure 2. In a smooth–walled pore (Figure 2a), the fluid–wall interaction is only a function of the normal distance from the walls and in a structured pore (Figure 2b) the pore walls are made up of discrete atoms. The geometry of the slit pore mimics the situation in the surface force experiment where fluids are confined between mica surfaces and the disjoining pressure is obtained as a function of changing pore width, H. We restrict our attention to confined soft sphere fluids. Snook and van Megen,[10,11] have used Grand canonical Monte Carlo simulations to study thermodynamics of fluids under confinement. In a GCMC simulation a pore of fixed volume, is equilibrated with a bulk reservoir whose chemical potential (μ) and temperature (T) are fixed. These early GCMC simulations were used to illustrate the formation of discrete fluid layers

Figure 2: Schematic of a slit pore used in simulations studies. The pore is of finite width, H and infinite in the other two directions (a) Smooth walled pore, where the interaction potential between fluid and wall is only a function of the normal fluid-wall distance. (b) Structured pore, where the pore wall is made up of discrete atoms. Under appropriate conditions the fluid can expitaxially freeze in a structured pore.

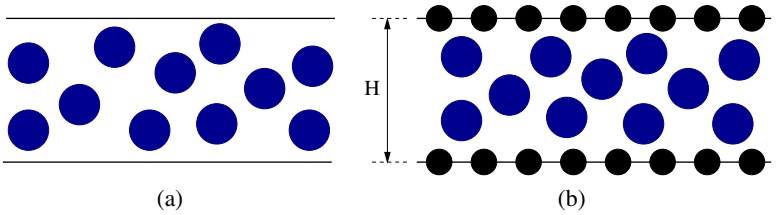

Epitaxial Freezing: Epitaxial freezing refers to a situation when atoms adsorbed on a substrate fit into the 3D corrugation formed by the underlying substrate atoms.

Landau–Ginzburg: Landau–Ginzburg free energy functional is an expansion in an appropriate order parameter which depends on the spatial co-ordinates of the system.

upon confinement and captured the accompanying oscillatory solvation pressure as a function of pore width. The solvation pressure is the normal pressure exerted by the fluid on the confining surfaces and is the quantity measured in surface force experiments. The solvation pressure is related to the grand potential of the system providing direct contact with the system's thermodynamics.[12–15]

Local order in the fluid, as revealed by the in-plane pair correlation functions, reveals that the pore fluid can epitaxially freeze if the confined fluid is commensurate with the atomic structure of the confining surface.[16,17] Alternate freezing and melting due to changing the relative registry between the two confining surfaces,[18–21] has been used to provide an atomic interpretation for stick-slip observed in surface force experiments.[22] The schematic of the structured pore in Figure 2b illustrates a situation when two opposing walls of the pore are in registry. Recent simulations in slit mica pores[23,24] have illustrated the influence of the surface registries as well as relative surface orientations on the structure of octamethylcyclotetrasiloxane, (OMCTS) a nonpolar organic molecule commonly used in force microscopy experiments.

Freezing of confined fluids has attracted considerable attention over the last decade and extensive reviews covering both the experimental and molecular simulations literature are available.[25,26] In particular the aforementioned reviews discuss the influence of confinement on structure and freezing temperature of a variety of fluids. These studies reveal that confinement can increase freezing temperature relative to the bulk for fluids with weak to moderate fluid–fluid interactions and strongly attractive walls such as mica and carbons. In the case of weakly attractive pores, the freezing temperature is reduced with respect to the bulk. A global phase diagram has been developed by Radhakrishnan et al.,[27,28] where the phase transition temperature (for Lennard-Jones fluids) is shown to depend on the reduced pore width, $H^* = H/\sigma_{ff}$ (where σ_{ff} is the fluid-fluid size parameter in the Lennard-Jones 12-6 potential); the ratio of diameters of the fluid-wall and fluid-fluid interactions as well as a dimensionless parameter, α which depends on the density of atoms on the wall, ratio of the fluid-fluid and fluid-wall interaction energies and spacing of wall atoms in the layers of atoms that comprise the pore wall. Simulations carried out over a wide variety of systems, reveal a useful qualitative relationship between the freezing temperature (relative to the bulk) and the parameter α. For values of $\alpha > 1$, pores are considered attractive and the freezing temperature is increased relative to the bulk. Free energy computations using the Landau-Ginzburg free energy method[29,30,27,28] reveal that the contact layers can be either crystalline or fluid-like depending on the strength of the fluid-wall interaction.

A recent aspect of freezing under confinement is the presence of solid–solid transitions which has marked similarities to the phase behaviour of confined colloids. Colloidal suspensions confined between glass plates in a wedge shaped geometry can form a variety of solid phases as the distance between the plates is varied. A sequence of transitions between triangular and square lattices is observed as the degree of confinement is increased.[31–33] For a fixed number of layers the square lattice precedes the formation of a triangular lattice. This sequence of transitions occurs with the addition of a new fluid layer. Recent GCMC simulations have shown that atomically confined soft sphere fluids in smooth walled pores can freeze and undergo a similar sequence of transitions from triangular to square lattices.[34–39] For a fixed number of layers the transition between square and triangular lattices is reflected in a splitting in the solvation pressure vs pore width relationship.[34,36] These studies illustrate that epitaxy is not a necessary condition for freezing. The striking similarity between the sequence of solid-solid transitions observed in the confined soft sphere systems with the earlier confined colloids indicate that packing effects play a major role in determining the state of confined fluids. In addition to triangular and square lattices, other phases made up of buckled (line or zig-zag), rhombic and prism structures have been observed in in simulations of confined hard spheres.[40–42,33,43,44] We have recently carried out an extensive study of

the structure of OMCTS confined in both smooth and stuctured mica pores, and observe that OMCTS undergoes a sequence of lattice transitions between triangular and square symmetry.[45] At small pore widths, we observe a linear buckled phase revealing a greater similarity with confined hard spheres.[41] The solid-solid transitions were observed upto three fluid layers, thereafter only solids with triangular symmetry form.

Molecular dynamics simulations of a soft sphere fluid confined between commensurate structured pores at the triple point illustrate split peaks in the disjoining pressure as a function of pore width.[46] The first peak in each pair is due to the formation of even numbered layers which are unable to freeze due to the commensurate nature of the walls and the second peak corresponds to a commensurately frozen phase made up of odd number of fluid layers. These results illustrate that splitting in the disjoining pressure peaks is not a unique signature of a solid-solid transition.[34,36]

Density functional studies[47,48] of freezing for confined soft sphere fluids capture the sequences of lattice transitions that are observed in GCMC studies. In the zero temperature density functional[48] analysis applied to the methane-graphite system, the predictions are in good agreement with earlier GCMC simulations of the same system.[35,36] In addition the theory predicts a stable zig-zag and line buckled phase. The study by Nguyen et al.,[47] illustrate that closed packed structures can effectively be used to predict adsorption capacities in the high pressure regime.

Unlike the hard sphere phase diagram, mapping the phase behaviour for confined soft sphere fluids in contact with a bulk reservoir is complicated. In addition to the state (T, μ) of the bulk reservoir, the state of the confined fluid, at a fixed pore width, is influenced by the fluid-wall interaction strength,[49,50] as well as the lattice spacing and atomic diameter of the surface atoms in the case of pores with atomically structured walls.[39] GCMC simulations of fluids confined in the bilayer regime, study the effect of varying the intensity of surface corrugation in a continuous manner.[39] The study illustrates the change in lattice symmetry from the square phase (present in the smooth wall) to a commensurate triangular phase at a fixed pore width. Phase diagrams in the $\mu - T$ plane map out the various phases in the bilayer regime. The study by Salamacha et al.,[50] where pores which accomodate 3-5 fluid layers are investigated, reveal the large number of possible structures that can form in pores with structured walls. In pores which can accomodate more than two layers the various modes of stacking adds to the variety of phases that can exist.[36,50]

2.1. *Fluids in Non-Uniform Nanopores*

Molecular simulation studies that concern the structure of fluids between non-uniform or hetereogeneous surfaces has received less attention when compared with the slit pore. In the case of geometric non-uniformity the local pore topology varies. The surfaces of the pores are constructed with grooves, wedges or other geometries giving rise to a distribution in the pore widths. In the case of chemical heterogeneity, the interactions between the confined fluid and the wall are varied in a prescribed manner. The influence of pore topology on the phase behaviour, fluid structure and dynamics is important in applications where contacting surfaces can be fabricated with a prescribed nanostructure.

The behaviour of monoatomic films have been investigated for a structured slit pore made up of one flat wall and the other corrugated with regularly spaced rectangular grooves.[51] The registry of the walls is seen to play an important role on the equilibrium structures that form under confinement. Under certain conditions, alternating strips of epitaxially induced solid and fluid can coexist. In a GCMC simulation where the grooves were varied in a continuous manner from a wedge to a rectangular shape,[52] capillary condensation was found to occur in the rectangular grooves and continous pore filling occured with the wedge shaped grooves. The influence of varying the interaction between the pore base, on which the grooves are created, relative to the interaction with the grooves, on pore filling mechanisms were investigated.

When the walls are made up of alternating strips,[53] differentiated from their interaction strength with the fluid; gas–liquid co-existence can be sustained in the pore, with liquid bridges supported between the strongly interacting strips. Registry between the weak and strong strips on alternating faces is required to observe co-existence. Liquid bridges can transform into nanodroplets and the transition to nanodroplets occurs via an intermediate liquid phase that fills the pore. The existence of the intermediate pore filling liquid phase depends on the strength of the fluid-wall interaction.[53] Phase behaviour and morphology of the liquid bridges in pore walls decorated with elliptic patterns to mimic the effect of chemical nanopatterning has also been investigated.[54] The influence of strain in fluids confined by chemically heterogeneous surfaces and the effect on phase behaviour and friction has been studied by Bock and co-workers.[55,56]

GCMC simulations of hard spheres confined in a slit pore whose walls are composed of periodic hard wedges,[57] indicate that the fluid is more ordered

in the corners when compared with fluid at the wedge tip. The influence of the height and angle of the wedge on the fluid structure in investigated. A density functional study[58] of fluid confined in a wedge shaped pore also shows a substantial increase in local density in the corners and is in good agreement with the study by Schoen and Dietrich.[57]

In a combined density functional and GCMC study by Frink and van Swol,[14] both pore walls are modelled by sinusoidal variations in the pore heights. The effect of a more realistic rough surface was investigated by using a tiled surface with a distribution of widths. Both forms of roughness reveal a decrease in the amplitude of the solvation force oscillations with increasing roughness. This decrease however was not found to be a monotonic function of the roughness. Grand potentials evaluated from the solvation force profile, were used to reveal the effect of surface corrugation and roughness on the global equilibrium pore width.[14]

Periodic surface roughness on the behaviour of confined soft sphere fluids is investigated by introducing unidirectional sinusoidal undulations in one wall of the slit pore.[15] The study reveals that the solvation force vs pore width relationship can be phase shifted in a systematic manner, with the phase shift controlled by the amplitude of roughness. Grand potential computations illustrate that interactions between the walls of the pore, can alter the pore width corresponding to the thermodynamically stable state, with wall-wall interactions playing an important role at smaller pore widths and higher amplitudes of roughness.

The studies on rough surfaces, reveals an interesting additive nature of the solvation force referred to as the superposition approximation, wherein the solvation force response from the prototypical slit pore with a uniform pore width, can be used to predict the solvation force response for a fluid confined between rough surfaces. The superposition approximation is found to be accurate, provided the wavelength of the roughness is sufficiently large.[14,59,15] The superposition approximation is similar in spirit to the Derjaguin approximation and assumes that the solvation force response between two curved surfaces is similar to that between two infinitely flat surfaces. The success of the superposition approximation in predicting the solvation force for pores with non uniform widths, depends on the ability of the fluid confined between surfaces of varying width, to exert local forces that are similar to those between infinitely flat surfaces. This requirement is related to the observation of solvation force oscillations in atomic force microscopy experments.[60] The studies, on the effects of roughness, reveal that fluids confined between rough or non-uniform surfaces, give rise to a positive shift in the solvation pressure and an oscillatory force response that is shorter ranged and damped when compared with smooth surfaces.[14,59,15]

The structure of soft spheres (spherically truncated and shifted 12-6 Lennard-Jones model) confined between a single wedge made up of structured walls, equilibrated with a bulk reservoir to acheive chemical equilibrium, has been studied using MD simulations.[61] The wedge angle is defined as the tilt of the pore wall from the horizontal slit pore configuration (Figure 2). For angles varying from 1–6° the normal pressure vs local pore width in the wedge was shown to have oscillations similar to that of the slit pore. However for a wedge angle of 6^o, the normal pressure oscillations were slightly damped when compared with the slit pore. The study also reveals that at small wedge angles a transition from square to triangular lattices is observed. This is similar to solid-solid transitions observed in confined colloids in a wedge geometry.[31] MD simulations have been used to study vapor nucleation in a structured slit pore composed of smooth[62] and structured walls.[63] In the study with structured pores one wall is strongly interacting and other weakly interacting with the vapor. The rate of heterogeneous nucleation on the smooth walled pores were found to be an order of magnitude slower when compared with the structured walls.[63]

2.2. *Diffusivity of confined fluids*

In addition to thermodynamics of confined fluids there have been a few studies concerned with analyzing the diffusivity of simple fluids under confinement in a slit pore geometry. We note here that the study of transport of confined inhomogeneous fluids, a subject not covered in this review, is a vast topic involving both equilibrium and non-equilibrium simulations as well as theory. We restrict our attention to the studies involving the self-diffusivity of confined fluids and their relationship to structure. The changes in self-diffusivity and interfacial tension of soft sphere fluids confined in slit pores have been studied using molecular dynamics simulations.[12] In these studies the pore densities are obtained from GCMC simulations and reflect the dynamics of the confined fluid in an open system, wherein the pore density reflects a system at equilibrium with an external bath. The oscillations in the self-diffusivity (parallel to the pore walls)[12,13] and interfacial tension[12] as a function of pore width reflect the formation and disruption of layers. In walls with structured surfaces, the degree of commensurability is seen to effect the magnitude of the oscillations in the self-diffusivity.[13] The effect of relative orientations between two mica surfaces on the self-diffusivity of the confined fluid has also been studied.[64]

Widoms test particle method: A particle isertion technique used widely in molecular simulations to determine the chemical potential of fluids

3. Fluids Confined in Carbon Nanotubes

Since its discovery by Iijima,[65,66] carbon nanotubes (CNTs) have attracted wide attention. Single walled carbon nanotubes (SWCNTs) can be constructed from a graphene sheet by specifying the direction of rolling and the circumference of the cross-section as shown in Fig. 3. The chiral vector $\mathbf{R} = n\mathbf{a_1} + m\mathbf{a_2}$ is defined on the graphene sheet by unit vectors $\mathbf{a_1}$ and $\mathbf{a_2}$. The integers n and m characterize the chiral vector, which are unique for a given SWCNT. In Fig. 3, the chiral vector $\mathbf{R}$ connects the two lattice points O and C. The dotted lines in the figure represent zigzag and armchair lines respectively. The chiral angle θ is the angle between the chiral vector $\mathbf{R}$ and the zigzag axis. Chirality has been shown to affect conductance, density, lattice structure and other properties.[67] Using simple geometry, the diameter, D, of a SWCNT and the chiral angle θ can be determined using the following relationships,[67]

$$D\,(\text{Å}) = 0.783\sqrt{n^2 + m^2 + nm} \qquad (1)$$

and

$$\theta = \arcsin\left\{\frac{\sqrt{3}m}{2\sqrt{(n^2 + m^2 + nm)}}\right\}. \qquad (2)$$

If $\theta = 0$, $(m = 0)$ the CNT is zig-zag, if $\theta = 30$, $(n = m)$ the CNT is armchair and $0 < \theta < 30$, $(n \neq m, m \neq 0)$ yields chiral CNTs.

Figure 3: (a) Construction of a SWCNT by different modes of rolling relative to the chiral vector $\mathbf{R}$. (Adapted from Wildoer et al.,[68]) Zig-zag CNTs are obtained when $\theta = 0$, $(m = 0)$, armchair when $\theta = 30$, $(n = m)$ and chiral when $0 < \theta < 30$, $(n \neq m, m \neq 0)$. The integers n and m uniquely specify the diameter (Eq. 1) and angle, θ (Eq. 2) of rolling. (b) Illustrates a (10,10) SWCNT in armchair configuration.

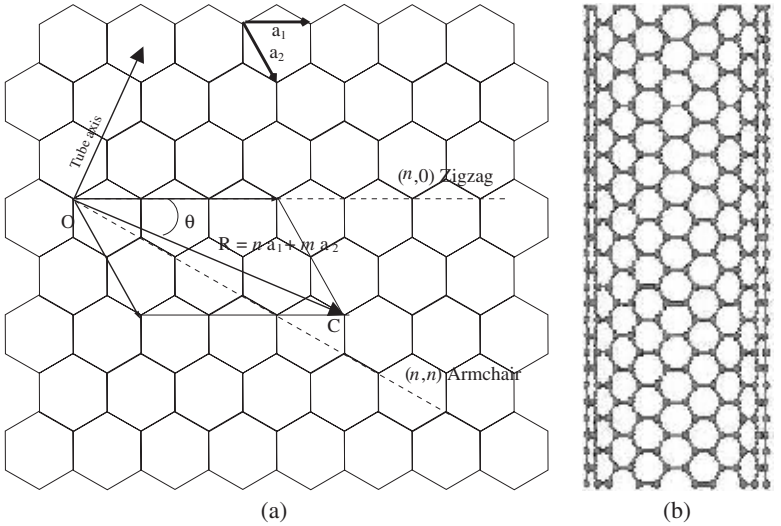

Due to their outstanding mechanical and electronic properties as well as their potential use in a number of novel nanotechnologies, CNTs have been extensively studied using both experiments and simulations. Applications of CNTs as (bio)molecule separation devices,[69–75] biocatalysis,[72] molecule detection and sensors,[76,77] storage and delivery,[78,79] proton storage and transport,[80] pores for rapid gas flows,[81] and nanopumps,[82] have been proposed or already demonstrated. In this review the emphasis is on molecular simulations studies that have been carried out to understand adsorption and transport of simple fluids in CNTs.

3.1. *Adsorption in Carbon Nanotubes*

Adsorption isotherms are typically used to characterize the thermodynamics of fluids confined in nanopores. The isotherm yields, at equilibrium, the amount of gas adsorbed in a given material at a fixed temperature. Adsorption isotherms provide the equilibrium uptake characteristics for materials used in designing industrial separation devices based on pressure or temperature swing adsorption and gas chromatography columns. The recent interest in nanoporous adsorbents as possible storage devices for hydrogen and methane is driven by the search for alternate sources of energy. In this regard the potential for using CNTs as a gas storage device has been explored using molecular simulations. The gas storage requirements set by the US Department of Energy (DOE) are 6–9 wt% for hydrogen and a volumetric target of 60–80 kg per cubic meter of adsorbent. An explicit review for hydrogen adsorption in CNTs is available in the literature.[83] MC simulations have been carried out to assess the influence of tube diameter and optimal configuration of tubes arranged in arrays or bundles of CNTs as shown in Fig 4.[84–87] These studies reveal that it is possible to exceed the proposed DOE storage targets of 6.5 wt% in optimally spaced arrays of CNTs at temperatures of 77 K and pressures in the range of 10 MPa. Arrays of 2.2 nm diameter SWCNTs optimally placed in square lattices were shown to yield adsorption capacities of 11.24 wt% and volumetric densities of 60 kg m^{-3} at 77 K and 10 MPa.[85] The excess adsorption capacity at 300 K is seen to vary linearly with pressure and did not exceed 1 wt% with pressures upto 17 MPa.[87] The low adsorption capacity at 300 K is in agreement with experimental results on a variety of carbon based adsorbents. Using a combination of the Widoms test particle insertion and a Langmuir isotherm model, alkali doping in arrays of SWCNTs is seen to increase the adsorption to 3.95 wt% and 4.21 wt% at 100 atm and room temperature for potassium and lithium ions respectively.[88]

Figure 4: Cross sectional arrangements of SWCNT arrays or bundles illustrating the tube diameter D, and the interstitial distance, d. (a) Square array (b) Triangular array.

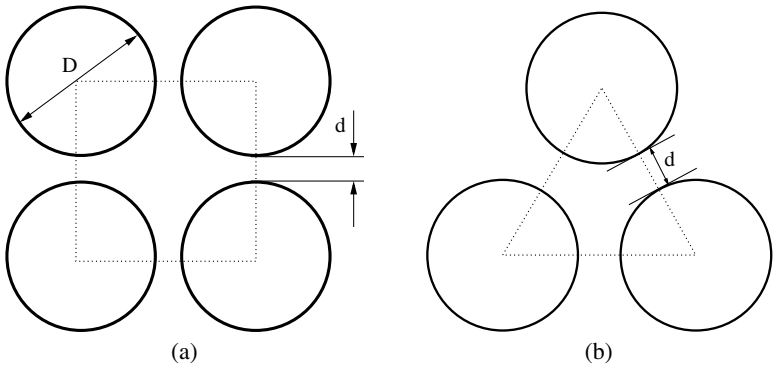

SWCNTs arranged in square lattices adsorb greater amounts of gas due to the increased accessible interstitial volume between the CNTs at lower temperatures. However at higher temperatures a hexagonal arrangement is more efficient since adsorption predominantly occurs near the carbon surface.[87,89] Multiwalled CNTs do not offer any advantage due to the increase in carbon to hydrogen weight ratios.[89]

An important aspect in studies of hydrogen adsorption are assessing the influence of quantum effects.[85,90–92] Comparison of adsorption capacities with and without quantum effects indicate that neglecting quantum effects can lead to an increase in the adsorption capacity by 20% at 77 K. At room temperature the differences are within 5%, indicating that quantum effects cannot be neglected.[90] Path integral MC simulations,[91] are in good agreement with the experimental liquid–vapour coexistence curve for bulk hydrogen in the temperature range 20–32 K. The liquid-vapor coexistence curve computed using Gibbs ensemble MC is much broader with a critical temperature overestimated by about 10 K.[91]

The molecular simulations literature on hydrogen adsorption in arrays of pure SWCNTs reveals that adsorption capacities at room temperature are below DOE targets. Although the targets are acheivable at lower temperatures and moderate pressures, the optimal array configurations predicted from simulations must be experimentally realizable. A recent combined quantum and classical simulaton with SiC nanotube arrays indicate that hydrogen adsorption at 175 K and 1 MPa pressure is greater by a factor of two when compared with a similar SWCNT array.[93]

3.2. *Water Adsorption*

Endohedral (inside the nanotube) adsorption isotherms of SPC/E(simple point charge/extended)[94] water in isolated SWCNTs have been studied by GCMC simulations.[95–97] Water adsorption is found to be negligible at low pressures and pore filling occurs primarily by capillary condensation, giving rise to a wide adsorption-desorption hysteresis.[95,96] Hysteresis loops were absent for (6,6;D = 8.1 Å) CNT at room temperature and 1D chain-like water structures were observed.[96] At a diameter of 10.8Å, water was seen to form a cubic phase filling the CNT at 298 K. At lower temperatures of 248 K an octagonal tubular structure of water was observed in a larger nanotube (D = 13.6Å).[96] The width of the hysteresis loop decreases with decreasing CNT diameter and increasing temperature. In the presence of carbonyl groups (C=O), which mimic activated carbons, adsorption isotherms are characterized by pore filling at lower pressure with narrower hysteresis loops when compared with pure CNTs.[97,98] The distribution of carbonyl groups has a strong effect on the adsorption and desorption isotherm. Pore filling occurs by the growth of clusters of hydrogen bonded water molecules near the carbonyl groups instead of formation of monolayers as observed in simple fluids.[96,98] These trends for water adsorption in CNTs with and without the presence of carbonyl groups, are qualitatively similar to those observed in slit carbon pores.[99,95] However, when compared with slit shaped graphitic pores, pore filling is seen to occur at lower pressures with narrower hysteresis loops in CNTs.

3.3. *Mixtures*

A few molecular simulation studies have been carried out to understand the potential of using carbon nanotubes for separation of mixtures. In a GCMC study of Lennard-Jones binary mixtures in SWCNTs, it is observed that the larger energetically favoured species is adsorbed at higher temperatures, however at lower temperatures and intermediate tube diameters the smaller species eliminates the larger species within the pore.[70] Size dependent selectivity has also been reported for Lennard-Jones mixtures in slit shaped mica pores where the larger species is able to eliminate the smaller species at particular pore widths.[100] Studies with the adsorption of linear and branched alkanes in carbon nanotube bundles show that long chain molecules are favoured at low pressures whereas shorter chains are adsorbed at higher pressure.[101] A high selectivity is observed for linear alkanes in a mixture of linear and branched chain alkanes.[101] Adsorption studies with mixtures of nitrogen and oxygen, in CNT

bundles, show that oxygen replaces nitrogen at high loadings due to a dominant entropic effect. Hence, high selectivity toward oxygen is observed at saturation loading.[102,74,75] For carbon monoxide and hydrogen mixtures, SWCNTs have a higher selectivity toward carbon monoxide over the entire pressure range decreasing with an increase in CNT diameter and interlayer spacing.[73]

3.4. *Dynamics and Transport*

Diffusion in CNTs has been widely investigated using molecular dynamics simulations. The quasi-1D nature of the CNTs has given rise to interesting and novel diffusion modes that are generally not observed in other nanoporous materials. Since the CNTs are finite sized in the radial direction, diffusive transport is observed only in the axial direction. Mean squared displacement of particles scales in the following manner as a function of time,

$$< |z(t) - z(0)|^2 > \propto t^{\alpha}, \qquad (3)$$

where z is the coordinate along the CNT axis and the brackets denote a time average. The value of α determines various regimes. The motion is ballistic when $\alpha = 2$, normal diffusion (long time limit) occurs when $\alpha = 1$. Single-file diffusion occurs when $\alpha = 0.5$. In addition molecular dynamics simulations reveal other intermediate regimes which are discussed below.

Molecular dynamics studies of methane, ethane and ethylene in SWCNTs of various diameters predict different diffusive regimes based on the values of α given in Eq. 3.[103,104] Single file diffusion is observed in the case of ethane and ethylene in 7.2Å diameter SWCNTs, however normal diffusive behaviour is observed for methane (spherical model) in the same nanotube.[103,104] Intermediate diffusive behaviour was observed for ethane and ethylene[104] where $0.5 < \alpha < 1$ in SWCNTs with diameters in the range 8–12.7Å. We note that in the above studies diffusion is measured in a non-equilibrium situation, where the molecules are allowed to diffuse through the nanotubes by imposing a high concentration of molecules at one end of an 80 Å long CNT. In this situation the pressure gradient, which is the driving force for transport varies during the course of the simulation. In addition the study also reveals that ethane and ethylene follow a spiral diffusive path along the nanotube walls.[104,105] Microcanonical MD simulations carried out for methane and ethane at low loadings[106,107] in SWCNTs of diameter 10.8Å observe a "superdiffusive" regime where $1 < \alpha < 2$. A value of $\alpha \approx 1.8$ was reported for methane and ethane in the SWCNTs. This superdiffusive behaviour has also been reported for the diffusion of oxygen in CNTs, albeit in a non-equilibrium situation.[108] Simulations of benzene in SWCNTs indicate that the motion is ballistic ($\alpha = 2$) for times as long as 300 ps.[109] Recent MD simulations, indicate that simulations times in 10s of ns, are required to observe normal diffusive behaviour in CNTs.[110,111] Microcanonical MD simulations of water in a 10.8Å nanotube support this view, indicating that even when single file motion is expected, normal diffusion is observed for simulation times exceeding 500 ps.[112]

The self diffusivities for hydrogen[81,113] and methane[81] along the axial direction in (6,6) and (10,10) carbon nanotubes are found to be about an order of magnitude greater (at high loadings) than that observed in equivalent diameter 1D channel siliceous zeolites such as ZSM-12 and silicalite.[81] It is observed that self-diffusivity decreases rapidly with increase in loading and pressure due to increased collisons.[81,114–116] The transport diffusivities in CNTs for both hydrogen and methane are found to be 3–4 orders of magnitude greater than in zeolite channels. In general the transport diffusivity is relatively insensitive to loading.[81,116] Recently it is observed that including the atoms of the CNT wall during the dynamics can play a crucial role in determining the self-diffusivity, and a thermostat has been suggested to incorporate this effect.[110,111] The influence of lattice flexibility is important in the low loading regime[110,117] where the increase in self-diffusivity obtained with a rigid CNT[81] is not observed with a flexible nanotube.

Comparison of both the self and transport diffusivities computed with a linear and spherical model for CO_2 in (10,10) CNTs reveals only marginal differences indicating that the spherical model provides an adequate description for CO_2.[116] Using a 5 site model for methane, it has been shown that rotational motion cannot be neglected and enhances the translational axial diffusivity in both $AlPO_4$-5 and SWCNTs.[106] The radial density distributions compared between a spherical and dumbbell model for diatomic fluids such as N_2 and Br_2 indicates little differences between the two models for nitrogen at both low and high loadings in SWCNTs.[118] However, the spherical approximation is less accurate for longer diatomic molecules such as Br_2 where the molecule can take different orientations near the wall.[118]

3.5. *Water in Carbon Nanotubes*

Structure and transport properties of water contained in CNTs have been investigated by a number of workers using molecular dynamics simulations. The focus has been primarily on

understanding the hydrogen bonding characteristics, possible new phases of confined water, as well as transport of water in the CNTs relative to bulk water. Prior to discussing the literature, we comment that the dynamics of the fluids within the CNT depends on the tube diameter as well as thermodynamic conditions at which the properties are studied. A natural means of fixing the density in the CNT is by performing a GCMC simulation wherein the chemical potential in the tube or bundle of tubes is equated with a bulk reservoir at a fixed temperature. In the absence of equilibrating the CNT with a bulk water, the density in the CNT has to be arbitrarily specified, and as seen with the slit pore simulations small changes in density could effect the structure and hence the dynamics of the confined fluid rather significantly.

Using MD simulations with a flexible SPC (simple point charge)[119] water model, axial diffusvities of water at a pore density of 1 gm cm^{-3} and 298 K confined in CNTs ranging in diameters from 4.1 to 6.8Å are higher (by about a factor of 1.5–2) than the bulk diffusivity of water. Increasing the temperature to 400 K results in a fivefold increase in self-diffusivity.[120] Self-diffusivities of water isotopes (D_2O) are slightly lower than water.[121] In the case of supercritical water confined in the CNTs, the self-diffusivities are reduced when compared with bulk supercritical water.[122] Reduced axial self-diffusivities of water relative to bulk water have been reported in MD simulations of rigid SPC/E water confined in CNTs ranging in diameter from 3.1–18.1Å and lengths of about 40Å immersed in water at 300 K.[123] In a 8.6Å diameter CNT, water is seen to form an ordered lattice comprised of stacks of cyclic hexamers, which form the unit cells for the I_h phase of ice.[123] Water in SWCNTs of 14Å diameter is seen to form a cubic ice-like phase.[124] MD simulations in SWCNTs of length 13.48Å immersed in a bath of TIP3P[125] (transferable interatomic potential-3 point) water showed the formation of single chain-like water structure at $D = 3.1$Å,[126] and report that differences between simulations where water was not adsorbed in a similar diameter nanotube,[127] could be attributed to differences between the oxygen-carbon interaction parameters. Furthermore, armchair and zig-zag CNTs showed little difference in the structure of water.[126] Using a rigd SPC model for water, Liu et al.,[128] report the formation of helical arrangements in a 13.6Å CNT. Additionally their study indicates that the axial diffusivity in CNTs ranging from 10.8-21.7Å in diameter for water densities in the range 0.875-1.25 g cm^{-3} is smaller than that of bulk water. The axial thermal and shear viscosities were found to be larger than that of bulk water[128] and increase sharply as the CNT diameter decreases.[129,130]

In a recent simulation study investigating water diffusion in SWCNTs the influence of simulation time on the self-diffusivity is critically evaluated for SPC/E water confined in a 10.8Å nanotube of length 148Å.[112] The pore densities are obtained from GCMC simulations. The mean squared displacement of the water molecules along the axial direction (Eq. 3) reveals a long lived ballistic regime lasting upto 0.5 ns. This is attributed to a persistent collective motion of the water molecules. 18 ns length simulations reveal that the ballistic regime is increased as water density in the CNT is reduced. This study does not capture the single file regime when particles do not pass each other (a requirement of single file behaviour) in the CNT. In comparison to the MD simulaton times typically used in the literature ($<1-2$ ns), MD simulations by Striolo[112] reveals the presence of the ballistic and normal diffusion regimes and stresses the importance of lengthy MD simulations to correctly interpret the dynamics.

Hydrogen bonding and its dynamics are also used to probe water structure and dynamics in CNTs. Using a flexible SPC/E water model, it is observed that confinement in a SWCNT the number of hydrogen bonds per water molecule (2.8–3.0) is less than that of bulk water (3.7) and this reduction is relatively insensitive to the CNT diameter in the range 10.9-16.3Å.[131,132] The reduction in hydrogen bonds, relative to bulk water, was greater in the case of supercritical water.[133] The relaxation of hydrogen bond correlation functions of SPC/E water in SWCNTs, is slower than that of bulk water, becoming slower as the CNT diameter decreases.[132] With the exception of the smallest CNTs ($D = 8.1$Å) the hydrogen bond lifetimes in CNTs are smaller than that of bulk water (0.8 ps).[132,134]

Pulsed water conduction through CNTs of 8.1Å diameter and 13.4 Å in length was observed for the first time by Hummer et al.,[134] who carried out MD simulations (66 ns duration) for a SWCNT immmersed in a bath of TIP3P water. The interaction parameter between water and carbon has a strong effect on water occupancy. With a small reduction in well depth (0.05 kcal mol^{-1}), a change from completely filled CNT, to a two state transition between empty and filled tube is observed.[134,135] A 1D continuous time random walk is able to quantitatively capture various features of the single file pulsed motion observed in MD simulations.[136] An electric field imposed along the tube axis shifts the equilibrium towards a filled state.[137] Simulations which include the dynamics of the CNT were reveal that lattice flexibility increases the hydrophobic character of the CNT by reducing its effective diameter. This decrease in effective

diameter decreases the mobility of water.[135] Water inside (6,6) CNT forms a water chain or wire, similar to situations that exist in biological systems.[80] An *ab initio* MD simulation performed with 6 water molecules confined in a (6,6) CNT illustrates that protonated water is more stable within the CNT than pure water and the excess proton is stabilized within the CNT. With an introduction of a small electric field along the tube axis the excess charge is delocalized and transports along the CNT.[80]

3.6. *Adsorption of Rare Gases in Carbon Nanotubes*

There are a few studies that are concerned with the adsorption of rare gases in CNTs. GCMC simulations of Xe at 95 K over a range of pressure is studied in SWCNTs.[138] The endohedral adsorption (inside the nanotube) as quantified by atomic Xe/C ratio of 0.06 in the CNT at 7×10^{-12} atm compares well with the experimental value of 0.042. For exohedral adsorption (outside the nanotube), a continuous transition from 2D cubic to 2D hexagonal lattice is observed with increase in pressure. Endohedral adsorption is dominated at low pressure followed by exohedral adsorption at high pressure in SWCNT.[138] Adsorption of argon in open ended SWCNTs bundles[139] proceeds first endohedrally, followed by formation of one-dimensional Ar chains in the grooves between the tubes. As the pressure is further increased, adsorption occurs in the endohedral axial sites followed by the formation of a two dimensional quasi-hexagonal monolayer at the outer surface of the bundles. A similar adsorption trend is observed in a separate study of nitrogen adsorption over a open ended SWCNTs bundle.[140]

Figure 5: Snapshot of C8 alkanethiol monolayer on gold obtained from a MD simulation performed in our laboratory using an united atom force field.[146] The tilt angle, $\theta = 25$, at 300 K.

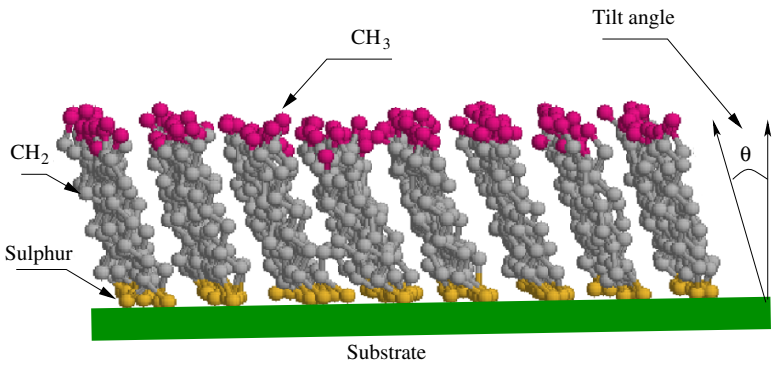

4. Self Assembled Monolayers

Self-assembled monolayers (SAMs) are formed when long chain molecules assemble into an ordered structure on a solid substrate as shown in Figure 5, which represents an atomic configuration obtained from an MD simulation peformed in our laboratory. Alkanethiol SAMs on Au were prepared by Nuzzo et al.,[141] when long chain thiol molecules were found to spontaneously chemisorb onto a Au substrate immersed in thiol solution. The monolayer is stabilized by the formation of the Au–S bond at the thiol–gold interface. In order to maximize van der Waals interactions between hydrocarbon chains, the chains are tilted at an angle (θ) to the surface normal. The tilt angle as defined in Figure 5 depends on the the lattice spacing and symmetry of the adsorption sites on the Au surface. Hence, SAMs on silver have a smaller tilt angle than SAMs on gold. The formation and characterization of SAMs on various substrates (Au, Ag and Si) have been extensively studied using a variety of experimental techniques, and a number of reviews concerned with this wide body of literature are available.[142–145]

The interest in the study of self assembled monolayers stems from potential technological implications, ranging from controlling surface properties such as wetting, adhesion, friction and adsorption. With the ability to create self assembled structures with molecules having a range of chemical specificity, these surface related properties can potentially be controlled and adapted for a suitable application. MD and MC simulations have been extensively used to study SAMs from an atomistic perspective and has contributed to a deeper understanding of the wide range of experimental data generated on these systems. The review in this section can be broadly classified into two parts. In the first part we focus on molecular simulations literature which probe various structural properties of SAMs that are commonly used to experimentally characterize these monolayers. In the second part, we discuss the simulations concerned with the adhesion and frictional properties of SAMs, as probed using scanning probe microscopes such as atomic and lateral force microscopy. Simulations are used to probe friction and adhesion as a function of chain length and terminal group chemistry. Some studies have also been carried out to study adhesion and friction between monolayers in the presence of an intervening fluid. Understanding friction at the atomic scale lies in identifying the various channels for energy dissipation and the recent literature has attempted to address this aspect in some detail. In what follows, we will use Cn to represent the number of carbon atoms, n, in the molecule used to form the monolayer.

Gauche defects: Gauche defects are determined from the dihedral angles sampled by the alkane chain and reflect the torsional disorder induced in the alkane chain as the temperature is increased.

4.1. *Alkanethiol SAMs*

In a pioneering study, MD simulations were used to investigate various structural and dynamical properties of alkanethiol ($SH(CH_2)_{15}CH_3$, C16) molecules arranged on a gold surface.[147–149] The force field comprised of an united atom representation, wherein the CH_2 and CH_3 groups are treated as single spherical entities, intramolecular bond bending, torsion potentials,[150,151] and rigid bond length constraints. For the interaction with the gold surface, a 1D interaction potential (12-3) is used and the van der Waals radius of the sulfur atom is adjusted to obtain a lattice parameter of 4.97 Å for the sulfur atoms on the gold surface. Using 90, C16 thiol molecules, these simulations are able to capture basic features of the monolayer, such as the film thickness and tilt angles in agreement (considering experimental erorrs of $\pm 10°$) with experiments. Simulations carried out with the terminal Au–S–C bond fixed at 100° revealed slower rotational relaxation and greater gauche defects as compared with the unconstrained Au–S–C bond.[147] The various phases that are observed as the monolayer is heated in the temperature range 50–500 K reveals an orientationally ordered solid, with a tilt in the nearest-neighbour direction at low temperatures (50–150 K). Between 200–275 K a locked rotator phase with a nearest-neighbour tilt directon is identified. Above 275 K rotation occurs freely as the chains untilt to angles below 10° with further heating. Gauche defect generation starts from the terminal CH_3 group (see Figure 5) and propagates into the monolayer toward the Au–S interface with an increase in temperature.[147,148] Differences between the low temperature lattice arrangements and those observed experimentally are discussed as well.[148] In contrast to the united atom model, an all atom simulation,[152] reveals next to nearest neighbour tilt directions, smaller tilt angles and slower orientational relaxation times. In addition, the tilt angle variation as a function of surface density is captured more accurately with the all atom model. Increasing the interatomic potential cut-off led to excellent agreement with the experimental data.[152]

Molecular dynamics simulations by Bhatia and Garrison[153] of alkanethiols adsorbed on a structured gold surface, whose atoms participate in the dynamics, capture a nearest neighbour to next to nearest neigbhour transition in the temperature range 40–300 K. Above 375 K a rapid increase in gauche defects, broadening of the relative azimuthal angle and tilt angle distributions are signatures of a melting transition. This study reveals that an all atom description of the alkanethiol chains is not a requirement for capturing the next to nearest neighbour tilt and some of the low temperature behaviour can be captured using a structured gold surface with a united atom aklanethiol model. Low temperature unit cells of the alkanethiol chains, that are compatible with the symmetries observed experimentally[154] are proposed by Bhatia and Garrision,[155] for both short and long chain alkanethiols. In an earlier study (with four different force fields) a purely energy minimization procedure was unable to identify the low temperature superlattice structures observed experimentally as the various structures were within 1 kcal/mol.[156] A model based on the formation of sulfur dimers has also been proposed to match the experimentally observed low temperature superlattice structures.[157]

A systematic study of the influence of system size on the monolayer property was carried out using MC simulations with 30, 90 and 224 molecules for the C16 system.[158] At 300 K the largest system was found to be less ordered with the formation of subdomains resulting in smaller tilt angles when compared with the smaller system sizes. Monolayer simulations using the configurational biased MC method, were used to study the effect of reduced carbon backbone flexibility (by constraining the C-C-C bonds of the carbon backbone) as well as the Au–S–C bond) and sulfur head group size on the structural and conformational properties of the C16 monolayer.[159]

In a combined experimental and MD study, comparing the thermal characteristics of short (C6, C8) and long (C18) alkanethiols (360 molecules) adsorbed on gold,[146] Gauche defect population in more defective short chains increase and saturate as the temperature is varied between 100–450 K. In contrast, the defect population continues to increase in the same temperature range, for the long chain alkanethiols. In the same study line defects, created by removing rows of thiol molecules from the gold substrate, led to greater tilt angles and more rapid defect accumulation when compared with the close packed monolayers. When the low temperature initial configuration had a large percent of gauche defects, annealing is observed in the temperature range 100–250 K. During this annealing stage, the percent of gauche defects reduced with increasing temperature.[146]

More recently a large-scale MD simulation involving a million atoms of C13 alkanethiol molecules on gold is investigated using an all-atom potential.[160] Monolayer properties as a function of chain length have also been investigated and compared with previous published results. The tilt angles for C13 show a saturation effect as a

function of temperature similar to that observed in the lower coverage (with line defects) C6 and C8 systems.[146] The results obtained in these large system simulations are in generally in good agreement with some of the earlier studies carried out with explicit gold atoms and significantly smaller systems.[153]

Properties of a united atom, alkanethiols on a structured (rigid) gold substrate with the sulfur atom covalently bonded to the three fold hollow site on the (111) gold surface, examine the differences in monolayer properties modelled using a flexible Au–S–C bond and a rigid Au–S–C bond.[161] The film thickness predictions from both models for C8-C15 alkanethiols are in good agreement with experiments. The tilt directions however are strongly influenced by the nature of the Au–S–C potential and a next-next to nearest neighbour tilt direction is observed at temperatures below 150 K with the flexible Au–S–C bond model.[161]

Molecular dynamics simulations have been used to explore structure and thermodynamics of C12, SAMs on 140 and 1289 atom gold clusters.[162] Compact monolayers are formed on the (111) and (100) facets with packing arrangements differing from the (111) infinite gold surface. Melting of monolayers is initiated at the boundaries of facets and propagates inwards. Melting temperatures of the adsorbed monolayers was 280 and 294 K for the smaller and larger crystallites respectively. These temperatures are lower than the melting temperature for SAMs adsorbed on an infinite gold surface.

Properties of alkanethiols on gold with CH_3, OH and C≡N[163] terminal groups has been compared using MD simulations. Incomplete hydrogen bonding between terminal OH groups leads to a glassy quasi-2D structure with a relatively large percentage of gauche defects at the terminal end of the monolayer. The C≡N terminated groups form an ordered ferroelectric structure which is incommensurate with the underlying triangular lattice formed by sulfur head groups on the gold substrate. In the same study, properties from an all atom model are compared with united atom models for monolayers.[163]

In addition to the alkanethiol on gold system that has formed the major focus of the molecular simulations literature, other self assembled system have also been investigated. These include monolayers of long chain perfluoro mercaptans on gold,[164] benzenethiolate and benzyl mercaptide on gold,[165] alkyl chains on mica,[166,167] 2-Rotaxanes on gold,[168] carboxylic acids monolayers,[169] and phosphorylcholine SAMs.[170]

4.2. *Mixed SAMs*

Mixed monolayers have the potential to form surfaces with properties that interpolate between the pure components. Hence surface properties such as adhesion, friction, adsorption and contact angle can be varied and controlled in a desired manner. Mixed monolayers of C10 and C20 alkanethiols on gold have been studied with MC simulations.[171] Simulations are carried out for 1:4, 1:1 and 4:1 ratios of large to short alkanethiol molecules. Results show that the mixture segregates forming co-existing domains of long and short molecules. The long chain thiols are more disordered than the short chains, forming terminal loops to increase van der Waals interactions with the short chain thiols. Phase segregation of long chains is more pronounced in the 1:4 (large to short) mixture when compared with the ability of short chains to segregate in the 4:1 mixture. This is due to the increased energetic benefit obtained when long chains aggregate. MC simulations of alkanethiol mixtures (C10–C20) on gold[172] in a 1:1 ratio indicates that segregation into domains is favoured when the difference between chain lengths exceeds 3 carbon atoms.[172]

Adsorption of two model protiens, cobra cardiotoxin (CTX) and protein E6, on mixed (C5 and C9) alkanethiol monolayers[173] are studied using MD simulations. The simulations show that the orientation of protein molecules depends on the composition of the SAM mixture, suggesting that binding affinities and protein orientation on the SAM can be tuned by suitably choosing the mixture composition. In this study mixed SAMs were prepared by randmonly placing thiols of different chain lengths on the gold surface to preventing segregation of chains.

4.3. *Adhesion and Frictional Properties of SAMs*

There have been several studies concerned with elucidating the molecular origins of friction on self assembled monolayers. In these studies a tip or surface is either moved normal to the surface of the SAM to study adhesion or indentation, or slid in a tangential directon across the SAM at a fixed normal load to study friction. The strength of adhesion is obtained from the depth of the minimum in the normal force vs distance curve. The friction coefficient, obtained by applying Amontons law, is the ratio of the frictional force to the normal load. In order to compute the frictional coefficient, simulations have to be performed over a wide range of normal loads. Most simulations, however typically report the friction force for the monolayer. Both quantitative and qualitative comparisons are made with available experimental literature where possible.

Monte Carlo simulations have been used to study the mechanical relaxation of C16 thiol SAM confined between two gold surfaces[174] to mimic the situation encountered in force microscopy.[175] The simulation is carried out by compressing a C16 SAM from 30 Å to 18.5 Å as measured by the distance between the two gold surfaces. This amounts to a 75% compression of the monolayer. At a distance of 23 Å between the two surfaces, a jump to contact point is inferred by a sharp drop of 5^o in the tilt angle indicating that the monolayer is elongated, accompanied by an increase in the attractive force. Further compression leads to an increase in tilt angle and a sharp repulsive force regime. On uncompressing, the weak hysteresis leads one to conclude that the process of indentation is mostly elastic. Similar qualitative features are observed during the compression of C16 alkanethiols by a flat counterface made up of discrete atoms.[176,177] The nature of forces during compression with a tapered aspertity made up of six atomic layers with a height of 15 Å was also investigated.[177] The asperity is able to penetrate closer to the gold surface, when compared with compression using a flat (structured) surface, by creating a large number of gauche defects within the vicinity of the asperity. Upon compression with loads in the μN range the two dimensional hexagonal lattice structure is seen to transform into a rhombic lattice with sulfur atoms shifting from the three fold lattice sites on the gold substrate to bridge sites.[177] Bonner and Baratoff[178] performed friction and adhesion simulations on a C11 alkanethiol SAM on gold. To mimic scanning force microscopy experiments, a pyramidal deformable tip connected by orthogonal springs to a rigid support is used. In addition to the first attractive minimum as the tip is moved toward the monolayer, the repulsive part of the normal force is non-monotonic. Upon retracting the tip a large hysteresis is observed. This is in contrast with earlier simulations with a rigid tip where smaller hysteresis is observed.[176,174]

C8, C13 and C22 hydrocarbon monolayers chemically bound to the (111) face of diamond are compressed with a counterface made up of a hydrogenated terminated (111) face of diamond.[179] The gauche defects, which accumulate primarily near the CH_3 end of the monolayer, tend to saturate with increased load. A significant increase in gauche defects is seen on releasing the load and with time these defects are gradually removed. In the same study, sliding friction simulations indicate that friction force is positively correlated with the fraction of gauche defects. Shorter chains with a higher precentage of gauche defects result in a higher friction force.[179] In a later study with C18 monolayers, Mikulski and Harrison[180] examine the differences in friction between fully covered monolayers and monolayers with 30% lower coverage, creating greater disorder in the monolayer. At low loads ($<$ 300 nN) the friction force is insensitive to the level of disorder, however at higher loads the friction force at a given load is lower for the fully covered, tightly packed monolayer. The various possible modes, such as gauche defect generation, torsional angle changes and bond vibration, and their contribution to energy dissipaton are evaluated.[180] MD simulations of an amorphous carbon tip sliding on SAMs (0–20 nN normal load) made up of 100 linear hydrocarbon chains covalently bonded to the (111) surface of diamond is used to study friction.[181] The carbon tip is prepared by quenching a liquid hydrocarbon mixture resulting in an amorphous hydrogen terminated tip with radii of curvature of about 45 Å. Pure C14 monolayers always showed lower friction force when compared with randomnly mixed C12 and C16 monolayers. Contact forces as measured by the net force exerted by the monolayer on the tip, reveal that for the pure monolayer, differences between positive (opposing sliding) and negative forces on the tip, that increase and decrease friction respectively, is small, resulting in good recovery of mechanical energy and hence lower friction. In contrast differences between the positive and negative forces are larger for mixed monolayers where higher friction is observed. A reorientation of the monolayer tilt during sliding was also observed.

Adhesion and friction between alkylsilane monolayers (C6–C18) on silicon dioxide surfaces is examined using MD simulations.[182] In contrast to alkanethiol SAMs, the alkylsilane monolayers adapted a configuration that is nearly normal to the substrate. Adhesion simulations carried out by moving the two monolayers toward each other reveals an attractive minimum yielding an adhesive force of about 150 MPa and a monotonic dependence of the pressure-distance curve on chain length. Stick slip, due to the possible commensurate configuration of the monolayers, is seen in the shear stress measured during sliding at low (0.1 m s^{-1}) and high velocities (10 m s^{-1}) of the monolayers in opposite directions. System size effects with 100–1600, C6 chains per surface reveal that the dynamics are relatively system size independent with the sharpness of stick-slip transitions decreasing with increasing system size. At high pressures the friction coefficient is independent of chain length and sliding velocity. However at low pressures the friction coefficient scales logarithmically with the sliding velocity for a fixed chain length.[182]

Difference in the adhesion and friction between CH_3, OH and COOH terminated, C8 alkanethiol

SAMs on gold, reveals that the adhesive force computed between two opposing monolayers with similar terminal groups is weakest for the CH_3 system when compared to the OH and COOH groups (higher surface energies) due to hydrogen bond formation in the latter.[183] Hysteresis, as observed in the normal force–distance curves, was the least for the CH_3 terminated SAMs. The qualitative trends in the tilt angle during compression are similar to those observed in a previous study where a gold substrate was used to compress a C16 alkanethiol monolayer on gold.[174] Friction between two monolayers revealed that the shear stress was the largest for the COOH terminated monolayers.[183] With fluorine terminated ($S(CH_2)_8CF_3$) alkanethiol monolayers on gold the friction between the monolayers reveal similar adhesive interactions to the CH_3 terminated SAM, albeit with a longer range of repulsion.[184] Simulation carried out by removing the Couloumb interaction for the CF_3 group, revealed that the origin of the long range repulsion was dominated by van der Waal interactions. In accordance with experiments, the shear stress and coefficient of friction was larger for the fluorinated SAMs.[184] The effect of disorder, introduced by randomnly removing chains and lowering the coverage by 10–30%, on the friction between alkylsilane monolayers on silicon reveals that in the presence of defects, the friction coeffecient and friction force are independent of chain length (C8, C12, C18). For fully covered monolayers the friction force showed a nonmonotonic dependence on the chain length, with C6 and C18 chains having higher friction coefficients than C8 and C12 chains.[185]

There have been a few molecular simulations that investigate adhesion and friction between SAMs in the presence of an intervening fluid.[186,187] Sliding friction between C9 alkyl monolayers on silicon with CH_3 terminated groups were compared with mixed monolayers 50% OH and 50% CH_3 for different levels of humidity and interface separations ranging from 4–9 Å as measured from the distance between opposing planes of the terminal groups. In all cases the friction coefficient for the CH_3 terminated SAMs was smaller and independent of humidity. In contrast mixed monolayers showed higher friction coefficients and a decrease of friction with humidity. Water was found to layer between hydrophilic surfaces (mixed monolayer) leading to a greater rise in the normal force when compared to the friction force as the humidity was increased.[186] In the presence of nonpolar intervening fluids such as n-decane friction coeffecients between hydrophobic and hydrophilic surfaces were quite similar.[187]

While probing dynamical processes such as friction using MD simulations the nanosecond time scale simulations (Figure 1) restricts the simulation to be carried out with high sliding velocities, typically 10s of m s^{-1}. In contrast the sliding velocities in experiments are 5–6 orders of magnitude smaller. In an effort to bridge these time scales, a hybrid simulation method is developed by Jiang and co-workers wherein the tip motion occurs on the order of microseconds and atoms of the monolayers are assumed to evolve quasistatically within typical nanosecond time scales set by conventional atomistic MD simulations.[188,189] The monolayer configuration is computed for every new position of the faster moving, larger mass tip. We note however, that the length scales for the monolayer are similar to those used in earlier simulations. Using these hybrid simulations with a pyramidal gold tip and sliding speeds in the range of 40 μm s^{-1} over alkanethiol SAMs on gold, the effective shear modulus is found to be chain length dependent with shorter chains (C8) showing larger friction than the longer chains (C15) with normal loads in the 1 nN regime. The elastic modulus from indentation studies is chain length independent for C8–C15 alkanethiols. Using a Hertzian contact the Youngs modulus of the SAM is estimated to be 20$\pm$ 10 GPa.[188]

Chemical force microscopy wherein the tips and substrates that are brought into contact during atomic force microscopy measurements are chemically modified with appropriate self assembled monolayers, has been simulated using MD simulations.[190,191] These simulations[190] with the hybrid simulation method developed earlier[188] and tip velocities of 40 μm s^{-1} show that the force of adhesion is 0.9 nN and 4.42 nN between CH_3 (C8) and OH (C7) terminated SAMs respectively. Significant elongation of the normal spring in adhesion simulations was observed during the pull-off stage and a large hysteresis typically observed in experiments is seen. Friction force was larger for the OH terminated SAMs. MD simulations with CH_3 terminated, C13 SAMs using conventional MD time scales for tip velocities (2 m s^{-1})[191] and full equilibration at each height, reveal little hysteresis, except at large separations, during the loading and unloading cycles. An adhesive force of 4.8 nN was obtained in these simulations and the SAM film underwent a solidifcation transition during compression. Application of the commonly used contact mechanics models to relate the contact radius to the normal load is investigated and reasons for deviations from these models is critically evaluated.[191]

Wear characteristis,[192] of C16 alkanethiols on a rigid structured gold substrate has been studied using MD simulation. A pyramidal rigid tip made

Fluctuation-dissipation: Fluctuation-dissipation theorems arise in statistical mechanics of systems at equilibrium, where the fluctuating forces are balanced by an appropriate dissipation. The balance between the two forces establishes the temperature in a DPD simulation.

Figure 6: Atomic configuration of a lipid bilayer obtained using DPD simulations performed in our laboratory. The lipid is made up of single tail surfactants with 1 head bead and 9 tail beads. The parameters are similar to those used in the study by Kranenburg and Smit.[195] Color code: Orange - Water, Blue - Surfactant headgroup, Green - Surfactant tail.

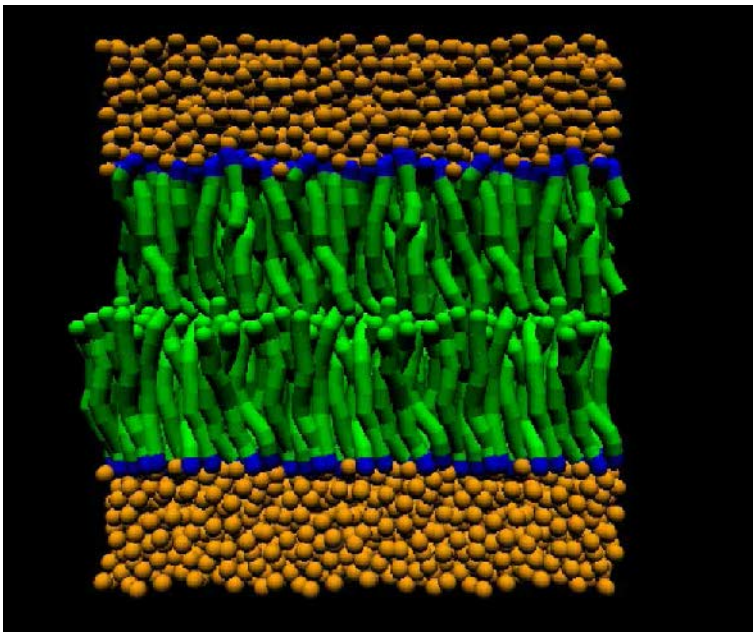

up of either silicon or carbon atoms is used. The tip is pushed down on a pre-equilibrated monolayer till contact occured with the substrate atoms. Then tip is moved on the surface along the $(11\bar{2})$ direction at constant vertical displacement and a velocity of about 200 m s^{-1} covering a distance of 11.4 nm during the simulation time of 60–100 ps. The results reveal that due to strong interchain interactions molecules are pushed and dragged along the surface. Influence of tip shape was investigated and at high tip velocities the width of the pattern increased due to the smaller time for relaxation and rearrangement of the molecules on the surface.[192] Non-contact mode atomic force microscopy has also been simulated using molecular dynamics. In these studies the monolayer is represented as a single layer of CH_3 atoms adsorbed on a substrate.[193,194]

5. Mesoscale Simulations: Dissipative Particle Dynamics

Figure 1 illustrates the relevant length and time scales that fall within the purview of mesoscale simulations. Many soft condensed matter systems such as polymers, oil–water–surfactant mixtures and proteins, often referred to as complex fluids fall into this class of mesoscale systems. A common feature in these systems is the coupling between the microscopic (molecular) and macroscopic structures. For example, in the case of self assembling systems, the aggregation behaviour arises from the competing volumes of hydrophilic and hydrophobic entities giving rise to structures such as micelles and bilayers. A successfull mesoscopic simulation seeks to bridge the connection between relevant microscopic and macroscopic phenomenon making it possible to observe mesoscopic system properties in a computationally efficient manner. We focus on one of the mesoscopic simulation techniques known as dissipative particle dynamics (DPD) which has been used to study polymers, oil–water–surfactant systems and continuum hydrodynamics. A snapshot of a lipid bilayer configuration obtained using DPD simulations in our laboratory is illustrated in Fig. 6 DPD was first developed and introduced by Hoogerbrugge and Koelman[196,197] in order to study hydrodynamics. The DPD particles interact via conservative, dissipative and random forces. All the forces are central and pairwise additive in nature, as in a classical atomistic MD simulation. The relationship of the original algorithm and its equivalent Fokker–Planck representation was established by Ēspanol and Warren[198] in order to derive a fluctuation dissipation theorem relating the strength of the random and dissipative forces. At equilibrium the system was shown to be equivalent to the

canonical ensemble phase space distribution. The canonical ensemble, is characterized by a constant number of particles, volume and temperature. Thus DPD as a thermostat was established. Unlike other mesoscopic simulation techniques such as lattice gas and Lattice Boltzmann simulations, DPD is performed in continuous space and time, yielding an algorithm that conserves both momentum and mass. Hence, DPD is a momentum conserving thermostat providing a direct route to system hydrodynamics. For completeness we present the basic governing equations for DPD.[198,199] For an N particle system the equations of motion are:

$$\begin{aligned} \dot{\mathbf{r}}_i &= \mathbf{v}_i \\ \dot{\mathbf{v}}_i &= \sum_{j>i}^{N} \sum_{i=1}^{N-1} \mathbf{F}_{ij} \end{aligned} \tag{4}$$

where $\mathbf{F}_{ij}$ is the total force between the particles i and j. There are three distinct forces acting in a DPD simulation. These are the conservative, dissipative and random forces. The interaction between two particles can be written as the sum of these three forces,

$$\mathbf{F}_{ij} = \mathbf{F}_{ij}^C + \mathbf{F}_{ij}^D + \mathbf{F}_{ij}^R, \tag{5}$$

where $\mathbf{F}_{ij}^C$ is the conservative force, $\mathbf{F}_{ij}^D$ the dissipative force and $\mathbf{F}_{ij}^R$ the random force. The conservative force

$$\mathbf{F}_{ij}^C = -\frac{\partial \phi_{ij}}{\partial \mathbf{r}_i}, \tag{6}$$

has the usual form of a gradient of a scalar potential. The dissipative force,

$$\mathbf{F}_{ij}^D = -\gamma w_D(r_{ij})[\mathbf{e}_{ij} \cdot \mathbf{v}_{ij}]\mathbf{e}_{ij}, \tag{7}$$

where γ is the strength of the dissipative force and $w_D(r_{ij})$ is an appropriate weighting function. $\mathbf{e}_{ij}$ is the unit vector in the direction of the vector $\mathbf{r}_{ij}$ and $\mathbf{v}_{ij}$ is the relative velocity between particles i and j. The negative sign indicates that the dissipative force opposes the relative velocity between two particles. The random force,

$$\mathbf{F}_{ij}^R = \sigma w_R(r_{ij}) \mathbf{e}_{ij} \theta_{ij}, \tag{8}$$

where σ is the strength of the random force with weighting function $w_R(r_{ij})$. Both the weight functions in the dissipative and random force vanish for $r > r_c$ where r_c is the cut-off radius. θ_{ij} is a random number with Gaussian statistics:

$$\begin{aligned} \langle \theta_{ij}(t) \rangle &= 0 \\ \langle \theta_{ij}(t) \theta_{kl}(t') \rangle &= \delta(t-t')(\delta_{ik}\delta_{jl} + \delta_{il}\delta_{jk}), \end{aligned} \tag{9}$$

We note that the form of the pair potential used in the conservative force, ϕ_{ij} and the weighting functions are not specified by the model itself. The conservative force, that is most often used is of the soft repusive form,

$$\mathbf{F}_{ij}^C = \begin{cases} a_{ij}\left(1 - \frac{r_{ij}}{r_c}\right)\mathbf{e}_{ij} & r_{ij} < r_c \\ 0 & r_{ij} \geq r_c \end{cases} \tag{10}$$

where a_{ij} is the repulsion parameter. The weight function in the dissipative force is also chosen to be of the same form as the soft repulsion used in the conservative force,

$$w_D(r_{ij}) = w_R^2(r_{ij}) = \begin{cases} \left(1 - \frac{r_{ij}}{r_c}\right) & r_{ij} < r_c \\ 0 & r_{ij} \geq r_c \end{cases} \tag{11}$$

From the definition of the above potentials the only length scale is r_c, the forces are central and conserve momentum, but not energy. In the absence of dissipative and random forces, the algorithm reduces to that of conventional MD simulations sampling configurations in the microcanonical ensemble. By enforcing the condition of canonical equilibrium (constant temperature), the relationship between the random and dissipative forces results in the following fluctuation-dissipation relationships,[198]

$$w_D(r_{ij}) = w_R^2(r_{ij}) \tag{12}$$

and

$$k_B T = \frac{\sigma^2}{2\gamma} \tag{13}$$

5.1. *Parametrizing the DPD System*

One of the central issues concerning the applicability of DPD to real systems lies in obtaining appropriate parameters. In order to relate the DPD system to the system of interest, the parameters a_{ij}, σ and system density (which determines the level of coarse graining) have to be specified. Groot and Warren[199] established a method to estimate the repulsion parameter, a_{ij} (Eq. 10) using appropriate thermodynamic properties. In the case of a pure fluid, the repulsion parameter is determined from the compressibility of the system of interest, in this case water. This involves generating the pressure-density relationship for the coarse grained system evolving in a DPD framework, from which the compressibility is obtained. While fixing the repulsion parameter the density of the DPD system (which is a free parameter) has to be judiciously chosen.[200,201] Recently, this procedure was used to obtain the repulsion parameter for

Flory-Huggins: Flory-Huggins parameter characterizes the interactions in polymer solutions and determines whether polymer chains in a solvent, can swell, collapse or behave as non-interacting chains.

Lees-Edwards: Lees-Edwards refers to the implementation of boundary conditions in the dynamical simulation of sheared liquids in an infinite periodic system.

a DPD representation of a soft sphere Lennard-Jones fluid.[201] In the case of a binary (AB) liquid interface the repulsion parameters (a_{AB}) are related to the Flory-Huggins parameter of the solute.[199] The variation of the Flory-Huggins and repulsion parameters as a function of bead size, which determines the level of coarse graining, has also been investigated with the aim of computing interfacial tensions in a phase separated binary mixture.[202]

The parameter, σ in Eq. 8, determines the strength of the random force and γ the strength of the dissipative force is related to σ (Eq. 13). σ is usually fixed with a tradeoff between a sufficiently large timestep, and accuracy as measured by the ability to mantain a constant temperature. Higher values of σ lead to an artificial temperature rise.[199] Since the dissipative force depends on the velocity, the numerical integration scheme requires some attention. Various algorithms based on self consistent and non self-consistent integrators have been proposed.[199,203–205] The self consistent algorithms, where an iterative procedure is used to obtain convergence in the velocities and corresponding dissipative force at a given time step, perform better when compared with the non self-consistent integrators.[203,204] However, computational costs for self consistent integrators are greater. In order to have a balance between accuracy and computational costs, a modified velocity-Verlet algorithm[199] has emerged as one of the more popular integrators used in DPD. Among the various ways to determine the appropriate size of the timestep, the simplest method is to check the ability of the simulation to mantain a constant temperature.[203–206]

To obtain the physical units of time in a DPD simulation no standard scheme is available, although an expression relating the self-diffusivity to the strength of the dissipative force, temperature and density is derived based on a Langevin model.[199] Time scales have been fixed by matching the diffusion coefficient of one of the components[207] as well as by matching the kinematic viscosity.[201] For the simulation of lipid membranes, Venturoli et *al.*[200] used the temperature of the bilayer phase transition to obtain an appropriate energy scale. We observe that DPD can be used with other forms of the conservative potential and hence provides a natural route to predictive simulations. One such approach, which appears to hold promise, is based on using reverse Monte Carlo methods to develop a conservative potential to be used in the DPD simulation.[208] Since the potentials obtained from the reverse Monte Carlo procedure naturally possess an energy and length scale, the mapping to real units is readily carried out. A key feature to keep in mind while using other coarse grained potentials, and not the soft repulsive potential, is to ensure a sufficiently high level of coarse graining to take advantage of DPD to simulate complex fluids with the focus on the mescoscopic features.

5.2. *Hydrodynamics*

Because DPD is ideally suited to studying hydrodynamics, there have been many studies assessing the suitability of the method to simulate flow around rigid bodies such as spheres and cylinders. Furthermore, flows around simple geometries have a wealth of numerical and analytical results that can be used to for validation. In early application of DPD, steady 2D shear using Lees-Edwards boundary condition[209] was investigated by Hoogerbruge and Koelman,[196] who illustrate the independence of shear viscosity on the shear rate for relatively small system sizes. In the same study, the drag force on a square array of cylinders at low Reynolds numbers, reproduced the limit of Stokes drag as predicted from continuum theory. The effect of various levels of coarse graining on the flow properties of a Lennard-Jones fluid is studied using DPD simulations for laminar flow and flow past a cylinder.[201] In all cases, results from the DPD simulations are compared with the MD simulations. In the DPD simulations a bounce-back reflection (where velocity components are reversed post-collision) is applied and the conservative parameter for the fluid-wall interaction is adjusted to achieve a no-slip boundary condition.[210] The conservative parameter a_{ij} is determined from the compressibility, the time scale fixed using the kinematic viscosity and mass densities are matched with that of the Lennard-Jones fluid. In order to acheive a good match between MD and DPD simulations, a relatively low level of coarse graining, where the number of DPD particles is one third the number of MD particles is required. Density fluctuations at the wall in a laminar flow are in general higher when compared with the DPD results and consistent with earlier laminar flow results.[211] With the correct level of coarse graining, both the Laminar flow and flow past a 2D array of square cylinders is found to be in very good agreement with Navier-Stokes solutions.[211,201,212]

The drag coefficient is computed as a function of Reynolds number for flow past spheres represented as a collection of DPD particles.[213] At low Reynolds number where inertial effects are negleced Stokes limit is recoverd. At higher Reynolds numbers (<50) the drag coefficient is in good agreement with experimental correlations. Specular reflections between the sphere and fluid interface lowers the

drag coefficients. The influence of the sphere radius, which dictates the approach to the continuum suspended solid,[214] on drag as well as effects of other DPD parameters is also investigated. Rheological properties of dense particle suspensions has been investigated using DPD. Shear thinning behaviour of suspension of spherical particles is successfully captured,[214,215] and suspension viscosity for high and low shear rates is in agreement with experimental results.[214] For disks and rodlike suspensions, appropriate scalings of the viscosity with volume fraction are recovered.[214] In contrast to the study by Boek et *al.*,[214] suspended particles (solute) are not treated as collection of discrete spheres, by Pryamitsyn et *al,*[215] however particles are treated as a continuum and fluid is allowed to transmit shear to the particles.[216,217] Hence the method includes equations of angular momentum to account for added rotational degrees of freedom. Lennard-Jones interactions were used to treat fluid-particle and particle–particle interactions. The method is able to capture the onset of glassy dynamics with increasing particulate volume fractions and the shear rheology results, with a single adjustable parameter, compared well with Stokesian dynamics simulations.

The soft repulsion form of the conservative force (Eq. 10), can be suitably altered to model mutliphase systems which require gas and liquid co-existence. Using interaction potentials similar to those used in smoothed particle hydrodynamics a soft repulsion is combined with a long range attractive component to obtain gas–liquid co-existence,[212] and gradients in density are incorporated via a van der Waals equation of state to simulate interfaces.[218] With these modifications, liquid drops, capillary waves, and oscillating drops have been simulated.[212,218]

Implementation of wall or solid objects in DPD is an issue that needs to be addressed carefully. A simple way to incorporate a solid object is to locally freeze the portions of the fluid in order to represent the object.[214,213] To simulate a colloidal system, the frozen particles that make up the sphere are moved using rigid body equations of motion.[214] Due to the soft interaction potential, particles may penetrate the wall creating slip.[211] To prevent this, a higher wall density is necessary,[211] increasing the computational demand. Increasing the wall density tends to distort the flow field near the wall.[211] Revenga et *al.*[219] used three different types of reflection laws in 2D Couette flow. In specular reflection, the parallel components of the particle momentum are conserved and the normal component is reversed. Maxwellian reflection, in which the particle is reintroduced in the system, according to Maxwells velocity distribution centered at the wall velocity and bounce back reflection where all the velocity components are reversed. For large friction coefficients, all the reflection laws work well, but for small friction coefficients, specular and Maxwellian reflection produce slip, whereas the bounce back reflection creates an artificial temperature rise in one of the components.[219] It is interesting to note that all these approaches suffer from anomolous density fluctuations near the wall.[220] The density profiles show an increase in fluctuations with increasing the level of coarse graining for a Lennard-Jones fluid.[220] An adaptive boundary is also suggested[220] where the region near the wall is divided into bins. If the density obtained is higher than the desired density, the force contribution from the wall to the bin is reduced. Analogously, if the density is lower, then the force contribution from the wall is increased. The results obtained for laminar flow from this method are in very good agreement with Navier–Stokes results.[220]

5.3. *Polymers*

It is easy to construct a polymer chain in DPD simulations using simple bead-spring models. Earlier studies of dilute polymer solutions using MD simulations showed that the ratio R_g/L, where R_g is the radius of gyration and L is the simulation box length should be low (0.1 to 0.3) to minimize the effect of periodic boundary conditions.[221] The bead-spring model is quite similar to the Rouse-Zimm bead-spring model for polymers. However, the bead in the DPD simulations represents a coarse grained part of a polymer chain. To verify that the DPD model is indeed useful in capturing essential physical phenomena, the scaling exponents for the radius of gyration and the longest relaxation time were calculated.[222,221,223] For $\zeta = 0$, (ζ is the solvent quality parameter) the results were in good agreement with the Rouse-Zimm theory.[222,221] For good solvents ($\zeta < 0$), as well as for poor solvents ($\zeta > 0$), the scaling exponents were in agreement with the established theory. Extension of like chains under shear was found to agree with experimental studies, for small degree of coarsegraining.[223] However, it is clear that the effects of polymer–solvent interaction is most important in determining the extent of excluded volume and hydrodynamic effects.[221] The conformational relaxation function shows an exponential decay[222] for short chains, which is in qualitative agreement with the Rouse-Zimm relaxation spectrum. For a ten bead chain, only three relaxation modes were observed in linear relaxation modulus which is in contrast with the

Figure 7: Schematic representation of various phases that can form with lipd bilayers. The low temperature gel phases transform to the liquid crystalline L_α phase at higher temperatures. The transition is primarily driven by chain melting.

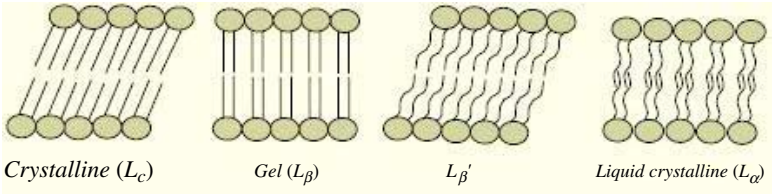

Rouse-Zimm model, where nine relaxation modes are obsered.[224] The shear thinning of the intrinsic viscosity and first normal stress coefficient with increasing shear rate are also captured.[224] The effect is more pronounced for the good solvent. Studies of the interfacial tension calculation in the simulation of the immiscible A/B homopolymer system show good agreement with the predictions from self consistent field theory.[225,226] However, the obtained interfacial thickness is larger when compared with the self consistent field theory predictions.[225] It is experimentally shown that the symmetric polymer(A_mB_m), forms a lamellar phase, if the Flory–Huggins parameter is large, whereas the asymmetric polymer(A_mB_n) does not form the lamellar phase. These results are also captured by DPD simulations,[226] and unstable phases such as gyroid phase, are not observed during the simulation.[226] For the ternary system with the third component as a block copolymer of the first two, the study shows the reduction in the interfacial tension.[225] Prediction of chain conformation in terms of an orientation order parameter are better than kinetic theory predictions when compared with light scattering data.[224]

5.4. ***Complex Phases in Water-Surfactant Systems***

DPD has been used to study various mesophases phases that are observed in oil–water–surfactant systems. Existence of various mesophases, such as the hexagonal, lamellar and isotropic phase are observed with a simple rigid dimer model in solution.[227] This model was found to qualitatively capture the experimental phase diagram of the non-ionic surfactant-water system, however the cubic and two phase (water-surfactant) regions were not observed. With the flexible dimer model where the strength of the hydrophilic interaction is evaluated, the model is also able to predict micelle formation.[228]

The phase behaviour of model lipid bilayers, has been investigated in great detail,[195,229,230] for both single and double chain lipids in the zero interfacial tension regime (using a combination of Monte Carlo moves). The beads that make up the tail have bond stretching as well as bond-bending potentials. The head groups are represented by a collection of 1-3 beads. For single tail chains a strongly interdigitated gel phase is observed at low temperatures and the extent of interdigitation reduced as the head–head repulsion parameter was decreased. An increase in the area per headgroup with temperature is in qualitative agreement with experimental data for smaller values of the head–head repulsion parameter.[195] In these studies the melting transition between the low temperature gel phases and the high temperature L_α phase (Figure 7) is investigated and phase diagrams as a function of the head–head repulsion parameter and temperature are presented. Simulations with double tail lipids[195,230] do not produce the low temperature interdigitated phase and the $L_{\beta'}$ phase characterized by tilted monolayers is observed. As the temperature is increased the $L_{\beta'}$ phase melts into the L_α phase. Adding an additional bead to the head groups (represented as three beads) was shown to increase interdigitation.[195] A more detailed study of the phase behaviour of double tail lipids reveals phase diagrams that capture the low temperatures L_c, L_β as well as the rippled phase which occurs in the transition between L_c, $L_{\beta'}$ and high temperature L_α phases. The dependence of chain length[230] and the addition of alcohol[229] on the phase diagrams are investigated in detail.

In other bilayer simulations, a three body bond angle potential is used to control the stifness of the hydrocarbon chain and this prevents the formation of the interdigitated phase over a wide range of tail lengths for single tail lipids.[231,232] The strength of this bond angle potential is necessary to obtain other phases,[233] as a function of tail length (degree of hydrophobicity). In the study of Li et al.,[233] in addition to spherical, cylindrical and disc-like micelles, reverse micelles, inverted hexagonal and bicontinous structures are also obtained using DPD simulations. The stress distribution in a

direction normal to the bilayer as a function of area per headgroup the corresponding interfacial tensions have been computed for a wide range of lipid architectures.[231,232] The stress distributions show marked similarities to those obtained using MD simulations, with the area stretch modulus increasing linearly with an increase in the tail length.[231]

The dynamics of vesicle (bilayer membrane encasing water) formation from a bilayer and an initial randomnly dispersed surfactant in solution have been reported.[234,235] Time taken for the vesicle to form was faster from an initial bilayer configuration when compared with a random initial configuration of lipids in water. Consistent with the experimental findings it is observed that vesicle formation is faster with double tail lipids. DPD has also been used to study the rupture of cell membrances by nonionic surfactants,[207] budding and fission dynamics during phase-separating bilayers,[236] influence of proteins on lipid bilayer structures[200] as well as membrane fusion.[237]

6. Summary and Perspective

Molecular simulation has proved to be a versatile and powerful tool to probe the structure and dynamics of systems from an atomic perspective. From the early computer simulations in the 50s and 60s on hard sphere systems, the development in both computing resources and advances in simulation techniques, enables us today to study systems with significantly increased complexity and scale. The review presents the breadth of systems that can currently be probed using molecular simulation techniques. The topics covered in this review represent systems of current scientific and technological importance, ranging from the behaviour of nanoscopically confined fluids, self assembled monolayers and a few systems at the mesoscale. The broad theme is the study of interfacial phenomenon and the technological implications range from catalysis, gas storage, atomic scale friction, membranes physics to detergency. We would like to note that computer simulations have played a unique role in the development of statistical mechanical theories of physical systems, a topic not covered in this review. An early example is the development of liquid state theories whose predictive accuracy was tested against molecular dynamics or Monte Carlo simulation data. Advances in the application of density functional theories to study the structure of simple fluids in a variety of confinement geometries covered in this review is yet another example.

Although atomistic simulations based on either empirical force fields or force fields derived from quantum chemical calculations have been used widely in studying systems ranging from the solid state to biology, the need to study complex mesophases and their dynamics and structure has led to the development of a variety of novel methods in the last decade. These methods are rooted in the ideas of coarse graining. Coarse graining allows one to study complex structures at the mesoscale as revealed by the literature on dissipative particle dynamics (Section 5), and essentially involves a reduction in the number of degrees of freedom of the original system. Whether this can be achieved in a consistent framework from a bottom-up approach, resulting in tractable equations for the evolution of coarse grained system dynamics, yet preserving the thermodynamics of the original system, is still an open question.[238,239]

In this review we have focused on simulation techniques that work well in any one single regime of length and time scales as depicted in the Figure 1. Clearly being able to bridge length and time scales across the various regimes is desired. This becomes important in many situations where the length and time scales probed in computer simulations are orders of magnitude different from the experiment, restricting one to make only qualitative predictions. We encountered one such situation in Section 4 where atomistic friction simulations using molecular dynamics, typically involve sliding speeds that are several orders of magnitude faster than those used in experiments. Hybrid simulations by Jiang[172] and co-workers illustrates a methodology for coupling different time scales to make contact with experiments. With advances in nanoscience based technologies in either biology or advanced materials the need for a unified approach, where the macroscopic structure and dynamics at the continuum level can be bridged with the atomic or electronic states of the molecules presents the big challenge.

Received 20 December 2006; revised 31 October 2006.

References

1. Metropolis, N., Rosenbluth, A. W., Rosenbluth, M. N., and Teller, A. H. Equation of state calculations by fast computing machines. *J. Chem. Phys* **21**, 1087–1092 (1953).
2. Alder, B. J. and Wainwright, T. E. Phase transition for a hard sphere system. *J. Chem. Phys* **27**, 1208–1209 (1957).
3. Wood, W. W. and Parker, F. R. Monte Carlo equation of state of molecules interacting with the Lennard-Jones potential. I. A supercritical isotherm at about twice the critical temperature. *J. Chem. Phys.* **27**, 720–733 (1957).
4. Rahman, A. Correlations in the motion of atoms in liquid argon. *Phys. Rev.* **136**, A405–A411 (1964).
5. Allen, M. P. and Tildesley, D. J. *Computer Simulation of Liquids*. Clarendon Press, New York, NY, USA, (1989).
6. Frenkel, D. and Smit, B. *Understanding Molecular Simulation*. Academic Press, Inc., Orlando, FL, USA, (2001).

7. Rapaport, D. C. *The Art of Molecular Dynamics Simulation*. Cambridge University Press, Cambridge, UK, (1995).
8. Leach, A. R. *Molecular Modelling : Principles and Applications*. Prentice Hall, (2002).
9. Haile, J. M. *Molecular Dynamics Simulation: Elementary Methods*. John Wiley & Sons, Inc., New York, NY, USA, (1992).
10. Snook, I. K. and van Megen, W. Solvation forces in simple dense fluids. I. *J. Chem. Phys.* **72**, 2907–2913 (1980).
11. van Megen, W. and Snook, I. Solvation forces in simple dense fluid. II. effect of chemical potential. *J. Chem. Phys.* **74**, 1409–1411 (1981).
12. Magda, J. J., M.Tirrell, and Davis, H. T. Molecular dynamics of narrow, liquid filled pores. *J. Chem. Phys.* **83**, 1888–1901 (1985).
13. Gao, J., Luedtke, W. D., and Landmann, U. Layering transitions and dynamics of confined liquids films. *Phys. Rev. Lett* **79**, 705–708 (1997).
14. Frink, L. J. D. and van Swol, F. Solvation forces between rough surfaces. *J. Chem. Phys.* **108**, 5588–5598 (1998).
15. Ghatak, C. and Ayappa, K. G. Solvation force, structure and thermodynamics of fluids confined in geometrically rough pores. *J. Chem. Phys.* **120**, 9703–9714 (2004).
16. Schoen, M., Diestler, D. J., and Cushman, J. H. Fluids in micropores.I.Structure of a simple classical fluid in a slit-pore. *J. Chem. Phys* **87**, 5464–5476 (1987).
17. Rhykerd Jr, C. L., Schoen, M., Diestler, D. J., and Cushman, J. H. Epitaxy in simple classical fluids in micropores and near-solid surfaces. *Nature* **330**, 461–463 (1987).
18. Schoen, M., Rhykerd Jr, C. L., Diestler, D. J., and Cushman, J. H. Shear forces in molecularly thin films. *Science* **245**, 1223–1225 (1989).
19. Thompson, P. A. and Robbins, M. O. Origin of stick-slip motion in boundary lubrication. *Science* **250**, 792–794 (1990).
20. Lupkowski, M. and van Swol, F. Ultrathin films under shear. **95**, 1995–1998 (1991).
21. Bordarier, P., Schoen, M., and Fuchs, A. H. Stick-slip phase transitions in confined solidlike films from an equilibrium prespective. *Phys. Rev. E* **57**, 1621–1635 (1996).
22. Gee, M. L., McGuiggan, P. M., and Israelachvili, J. N. Liquid to solid like transitions of molecularly thin films under shear. *J. Chem. Phys.* **93**, 1895–1906 (1990).
23. Curry, J. E. Structure of a model lubricant in a mica slit pore. *J. Chem. Phys.* **113**, 2400–2406 (2000).
24. Curry, J. E. The mica slit-pore as a tool to control the orientation and distortion of simple liquid monolayers. *Mol. Phys.* **99**, 745–752 (2001).
25. Gelb, L. D., Gubbins, K. E., Radhakrishan, R., and Sliwinska-Bartkowiak, M. Phase separation in confined systems. *Rep. Prog. Phys.* **62**, 1573–1659 (1999).
26. Alba-Simionesco, C., Coasne, B., Dosseh, G., Dudziak, G., Gubbins, K. E., Radhakrishnan, R., and Sliwinska-Bartkowiak, M. Effects of confinement on freezing and melting. *J. Phys.:Condens. Matter* **18**, R15–R68 (2006).
27. Radhakrishanan, R., Gubbins, K. E., and Sliwinska-Bartkowiak, M. Effect of fluid-wall interaction on freezing of confined fluids: Toward the development of a global phase diagram. *J. Chem. Phys.* **112**, 11048 (2000).
28. Radhakrishanan, R., Gubbins, K. E., and Sliwinska-Bartkowiak, M. Global phase diagrams for freezing in porous media. *J. Chem. Phys.* **116**, 1147–1157 (2002).
29. Radhakrishanan, R. and Gubbins, K. E. Free energy studies of freezing in slit pores:an order-parameter approach using Monte Carlo simulation. *Mol. Phys* **96**, 1249–1267 (1999).
30. Radhakrishanan, R., Gubbins, K. E., Watanabe, A., and Kaneko, K. Freezing of simple fluids in microporous activated carbon fibers: Comparison of simulation and experiment. *J. Chem. Phys.* **111**, 9058–9067 (1999).
31. Pieranski, P., Strzelecki, L., and Pansu, B. Thin colloidal crystals. *Phys. Rev. Lett.* **50**, 900–903 (1983).
32. van Winkle, D. H. and Murray, C. A. Layering transitions in colloidal crystals as observed by diffraction and direct-lattice imaging. *Phys. Rev. A* **34**, 562 (1986).
33. Neser, S., Bechinger, C., Leiderer, P., and Palberg, T. Finite-size effects on the closest packing of hard spheres. *Phys. Rev. Lett* **79**, 2348–2351 (1997).
34. Bordarier, P., Rousseau, B., and Fuchs, A. H. Solvation force and confinement-induced phase transitions of model ultra thin films. *Mol. Sim.* **17**, 199–216 (1996).
35. Ghatak, C. and Ayappa, K. G. Solid-solid transformations in a confined soft sphere fluid. *Phys. Rev. E* **64**, 051507 (2001).
36. Ayappa, K. G. and Ghatak, C. The structure of frozen phases in slit nanopores: A grand canonical Monte Carlo study. *J. Chem. Phys.* **117**, 5373–5383 (2002).
37. Ghatak, C. and Ayappa, K. G. Solid-solid transitions in slit nanopores. *Colloids and Surfaces A: Physicochemical and Engineering Aspects* **205**, 111–117 (2002).
38. Vishnyakov, A. and Neimark, A. V. Specifics of freezing of Lennard-Jones fluid confined to molecularly thin layers. *J. Chem. Phys.* **118**, 7585–7598 (2003).
39. Patrykiejew, A. and Sokolowski, S. On the structure of bilayer condensed phases confined between crystalline walls of triangular symmetry. *J. Chem. Phys.* **124**, 194705 (2006).
40. Hug, J. E., van Swol, F., and Zukoski, C. F. The freezing of colloidal suspensions in confined spaces. *Langmuir* **11**, 111–118 (1995).
41. Schmidt, M. and Löwen, H. Phase diagram of hard spheres confined between two parallel plates. *Phys. Rev. E* **55**, 7228–7241 (1997).
42. Fortini, A. and Dijkstra, M. Phase behaviour of hard spheres confined between parallel hard plates: Manipulation of colloidal crystal structures by confinement. *J. Phys.: Condens. Matter* **18**, L371–L378 (2006).
43. Marcus, A. H. and Rice, S. A. Phase transitions in a confined quasi-two-dimensional colloid suspension. *Phys. Rev. E* **55**, 637–656 (1996).
44. Zangi, R. and Rice, S. A. Nature of the transition from two-to three-dimensional ordering in a confined colloidal suspension. *Phys. Rev. E* **61**, 660–670 (2000).
45. Ayappa, K. G. and Mishra, R. K. Freezing in a mica slit pore. Submitted to *J. Phys. Chem. B* (2007).
46. Cámara, L. G. and Bresme, F. Molecular dynamics simulations of crystallization under confinement at triple point conditions. *J. Chem. Phys.* **119**, 2792–2800 (2003).
47. Nguyen, T. X., Bhatia, S. K., and Nicholson, D. Close packed transitions in slit-shaped pores: Density functional theory study of methane adsorption capacity in carbon. *J. Chem. Phys.* **117**, 10827–10836 (2002).
48. Bock, H., Gubbins, K. E., and Ayappa, K. G. Solid/solid phase transitions in confined thin films: A zero temperature approach. *J. Chem. Phys.* **122**, 094709 (2005).
49. Salamacha, L., Patrykiejew, A., Sokolowski, S., and Binder, K. The structure of fluids confined in cyrstalline slitlike nanoscopic pores: Bilayers. *J. Chem. Phys.* **120**, 1017–1030 (2004).
50. Salamacha, L., Patrykiejew, A., Sokolowski, S., and Binder, K. The structure of fluids confined in cyrstalline slitlike nanoscopic pores. *J. Chem. Phys.* **122**, 074703 (2005).
51. Curry, J. E., Zhang, F., Cushman, J. H., Schoen, M., and Diestler, D. J. Transient coexisting nanophases in ultrathin films confined between corrugated walls. *J. Chem. Phys.* **101**, 10824–10832 (1994).
52. Bohlen, H. and Schoen, M. Effect of fluid-substrate attraction

and pore geometry on fluid adsorption. *J. Chem. Phys.* **123**, 124714 (205).
53. Schoen, M. and Diestler, D. J. Ultrathin fluid films confined to a chemically heterogeneous slit-shaped nanopore. *Phys. Rev. E* **56**, 4427–4440 (1997).
54. Sacquin-Mora, S., Fuchs, A. H., and Schoen, M. Torsion-induced phase transitions in fluids confined between chemically decorated substrates. *J. Chem. Phys.* **121**, 9077–9086 (2004).
55. Bock, H. and Schoen, M. Shear-induced phase transitions in fluids confined between chemically decorated substrates. *J. Phys.: Condens. Matter* **12**, 1569–1594 (2000).
56. Bock, H., Diestler, D. J., and Schoen, M. Role of nanoscopic liquid bridges in static friction. *Phys. Rev. E* **64**, 046124 (2001).
57. Schoen, M. and Dietrich, S. Structure of a hard-sphere fluid in hard wedges. *Phys. Rev. E* **56**, 499–510 (1997).
58. Henderson, D., Sokolowski, S., and Wasan, D. Structure of hard sphere fluid near a rough surface: A density-functional approach. *Phys. Rev. E* **57**, 5539–5543 (1998).
59. Porcheron, F., Schoen, M., and Fuchs, A. H. Monte Carlo simulation of a complex fluid confined to a pore with nanoscopically rough walls. *J. Chem. Phys.* **116**, 5816–5824 (2002).
60. O'Shea, J., Welland, M. E., and Pethica, J. B. *Chem. Phys. Lett.* **223**, 336–340 (1994).
61. Camara, L. G. and Bresme, F. Liquids confined in wedge shaped pores: Nonuniform pressure induced by pore geometry. *J. Chem. Phys.* **120**, 11355–11358 (2004).
62. Yasuoka, K., Gao, G. T., and Zeng, X. C. Molecular dynamics simulation of supersaturated vapor nucleation in slit pore. *J. Chem. Phys.* **112**, 4279–4285 (2000).
63. Kholmurodov, K. T., Yasuoka, K., and Zeng, X. C. Molecular dynamics simulation of supersaturated vapor nucleation in slit pore. II. Thermostatted atomic-wall model. *J. Chem. Phys.* **114**, 9578–9584 (2001).
64. Su, Z., Cushman, J. H., and Curry, J. E. Computer simulation of anisotropic diffusion in monolayer films in mica slit pores. *J. Chem. Phys.* **118**, 1417 (2003).
65. Iijima, S. Helical microtubules of graphitic carbon. *Nature* **354**, 56–58 (1991).
66. Iijima, S. and Ichihashi, T. Single shell carbon nanotubes of 1-nm diameter. *Nature* **363**, 603–605 (1993).
67. Qian, D., Wagner, G. J., Liu, W. K., Yu, M. F., and Ruoff, R. S. Mechanics of carbon nanotubes. *Appl. Mech. Rev.* **55**, 495–533 (2002).
68. Wildöer, J. W. G., Venema, L. C., Rinzler, A. G., Smalley, R. E., and Dekker, C. Electronic structure of atomically resolved carbon nanotubes. *Nature* **391**, 59–62 (1998).
69. Jirage, K. B., Hulteen, J. C., and Martin, C. R. Nanotubule-based molecular-filtration membranes. *Science* **278**, 655–658 (1997).
70. Ayappa, K. G. Simulations of binary mixture adsorption in carbon nanotubes: Transitions in adsorbed fluid composition. *Langmuir* **14**, 880–890 (1998).
71. Miller, S. A., Young, V. Y., and Martin, C. R. Electroosmotic flow in template-prepared carbon nanotube membranes. *J. Am. Chem. Soc.* **123**, 12335–12342 (2001).
72. Mitchell, D. T., Lee, S. B., Trofin, L., Li, N., Nevanen, T. K., Soderlund, H., and Martin, C. R. Smart nanotubes for bioseparations and biocatalysis. *J. Am. Chem. Soc.* **124**, 11864–11865 (2002).
73. Gu, C., Gao, G. H., Yu, Y. X., and Nitta, T. Simulation for separation of hydrogen and carbon monoxide by adsorption on single-walled carbon nanotubes. *Fluid Phase Equilibria* **194-197**, 297–307 (2002).
74. Arora, G. and Sandler, S. I. Air separation by single wall carbon nanotubes: Thermodynamics and adsorptive selectivity. *J. Chem. Phys.* **123**, 044705 (2005).
75. Arora, G. and Sandler, S. I. Air separation by single wall carbon nanotubes: Mass transport and kinetic selectivity. *J. Chem. Phys.* **124**, 084702 (2006).
76. Deamer, D. W. and Akeson, M. Nanopores and nucleic acids: prospects for ultrarapid sequencing. *Trends Biotech.* **18**, 147–151 (2000).
77. Ghosh, S., Sood, A. K., and Kumar, N. Carbon nanotube flow sensors. *Science* **299**, 1042–1044 (2003).
78. Ajayan, P. M. and Iijima, S. Capillarity-induced filling of carbon nanotubes. *Nature* **361**, 333–334 (1993).
79. Ajayan, P. M., Stephan, O., Redlich, P., and Colliex, C. Carbon nanotubes as removable templates for metal oxide nanocomposites and nanostructures. *Nature* **375**, 564–567 (1995).
80. Mann, D. J. and Halls, M. D. Water alignment and proton conduction inside carbon nanotubes. *Phys. Rev. Lett.* **90**, 195503 (2003).
81. Skoulidas, A. I., Ackerman, D. M., Johnson, J. K., and Sholl, D. S. Rapid transport of gases in carbon nanotubes. *Phys. Rev. Lett.* **89**, 185901 (2002).
82. Insepov, Z., Wolf, D., and Hassanein, A. Nanopumping using carbon nanotubes. *Nano Lett.* **6**, 1893–1895 (2006).
83. Darkrim, F. L., Malbrunot, P., and Tartaglia, G. P. Review of hydrogen storage by adsorption in carbon nanotubes. *Int. J. Hydrogen Eng.* **27**, 193–202 (2002).
84. Darkrim, F. and Levesque, D. Monte Carlo simulations of hydrogen adsorption in single-walled carbon nanotubes. *J. Chem. Phys.* **109**, 4981–4984 (1998).
85. Darkrim, F. and Levesque, D. High adsorptive property of opened carbon nanotubes at 77 K. *J. Phys. Chem. B* **104**, 6773–6776 (2000).
86. Levesque, D., Gicquel, A., Darkrim, F. L., and Kayiran, S. B. Monte Carlo simulations of hydrogen storage in carbon nanotubes. *J. Phys. Cond. Mat.* **14**, 9285–9293 (2002).
87. Zhang, X., Cao, D., and Chen, J. Hydrogen adsorption storage on single-walled carbon nanotube arrays by a combination of classical potential and density functional theory. *J. Phys. Chem. B* **107**, 4942–4950 (2003).
88. Hu, N., Sun, X., and Hsu, A. Monte Carlo simulations of hydrogen adsorption in alkali-doped single-walled carbon nanotubes. *J. Chem. Phys.* **123**, 044708 (2005).
89. Cheng, J., Yuan, X., Zhao, L., Huang, D., Zhao, M., Dai, L., and Ding, R. GCMC simulation of hydrogen physisorption on carbon nanotubes and nanotube arrays. *Carbon* **42**, 2019–2024 (2004).
90. Darkrim, F., Aoufi, A., and Levesque, D. Quantum contribution to gas adsorption in carbon nanotubes. *Mol. Sim.* **24**, 51–61 (2000).
91. Gu, C. and Gao, G. H. Path integral simulation of hydrogen adsorption in single-walled carbon nanotubes at low temperatures. *Phys. Chem. Chem. Phys.* **4**, 4700–4708 (2002).
92. Tanaka, H., Kanoh, H., Merraoui, M. E., Steele, W. A., Yudasaka, M., Iijima, S., and Kaneko, K. Quantum effects on hydrogen adsorption in internal nanospaces of single-wall carbon nanohorns. *J. Phys. Chem. B* **108**, 17457–17465 (2004).
93. Mpourmpakis, G., Froudakis, G. E., Lithoxoos, G. P., and Samios, J. Sic nanotubes: A novel material for hydrogen storage. *Nano Lett.* **6**, 1581–1583 (2006).
94. Berendsen, H. J. C., Grigera, J. R., and Straatsma, T. P. The missing term in effective pair potentials. *J. Phys. Chem.* **91**, 6269–6271 (1987).
95. Striolo, A., Gubbins, K. E., Chialvo, A. A., and Cummings, P. T. Simulated water adsorption isotherms in carbon nanopores. *Mol. Phys.* **102**, 243–251 (2004).
96. Striolo, A., Chialvo, A. A., Gubbins, K. E., and Cummings, P. T. Water in carbon nanotubes: Adsorption isotherms and thermodynamic properties from molecular simulation. *J. Chem. Phys.* **122**, 234712 (2005).

97. Striolo, A., Naicker, P. K., Chialvo, A. A., Cummings, P. T., and Gubbins, K. E. Simulated water adsorption isotherms in hydrophilic and hydrophobic cylindrical nanopores. *Adsorption* **11**, 397–401 (2005).
98. Striolo, A., Chialvo, A. A., Cummings, P. T., and Gubbins, K. E. Simulated water adsorption in chemically heterogeneous carbon nanotubes. *J. Chem. Phys.* **124**, 074710 (2006).
99. Striolo, A., Chialvo, A. A., Cummings, P. T., and Gubbins, K. E. Water adsorption in carbon-slit nanopores. *Langmuir* **19**, 8583–8591 (2003).
100. Somers, S. A., McCormick, A. V., and Davis, H. T. Superselectivity and solvation forces of a two component fluid adsorbed in slit micropores. *J. Chem. Phys.* **99**, 9890 (1993).
101. Jiang, J., Sandler, S. I., Schenk, M., and Smit, B. Adsorption and separation of linear and branched alkanes on carbon nanotube bundles from configurational-bias Monte Carlo simulation. *Phys. Rev. B* **72**, 045447 (2005).
102. Jiang, J. and Sandler, S. I. Nitrogen and oxygen mixture adsorption on carbon nanotube bundles from molecular simulation. *Langmuir* **20**, 10910–10918 (2004).
103. Mao, Z., Garg, A., and Sinnott, S. B. Molecular dynamics simulations of the filling and decorating of carbon nanotubules. *Nanotechnology* **10**, 273–277 (1999).
104. Mao, Z. and Sinnott, S. B. A computational study of molecular diffusion and dynamic flow through carbon nanotubes. *J. Phys. Chem. B* **104**, 4618–4624 (2000).
105. Mao, Z. and Sinnott, S. B. Predictions of a spiral diffusion path for nonspherical organic molecules in carbon nanotubes. *Phys. Rev. Lett.* **89**, 278301 (2002).
106. Bhide, S. Y. and Yashonath, S. Orientational preference and influence of rotation on methane mobility in one-dimensional channels. *J. Chem. Phys.* **116**, 2175–2183 (2002).
107. Bhide, S. Y. and Yashonath, S. Study of translational and rotational mobility and orientational preference of ethane in one-dimensional channels. *J. Phys. Chem. A* **106**, 7130–7137 (2002).
108. Lee, K. H. and Sinnott, S. B. Equilibrium and nonequilibrium transport of oxygen in carbon nanotubes. *Nano Lett.* **5**, 793–798 (2005).
109. Bhide, S. Y. and Yashonath, S. Structure and dynamics of benzene in one-dimensional channels. *J. Phys. Chem. B* **104**, 11977–11986 (2000).
110. Jakobtorweihen, S., Verbeek, M. G., Lowe, C. P., Keil, F. J., and Smit, B. Understanding the loading dependence of self-diffusion in carbon nanotubes. *Phys. Rev. Lett.* **95**, 044501 (2005).
111. Jakobtorweihen, S., Lowe, C. P., Keil, F. J., and Smit, B. A novel algorithm to model the influence of host lattice flexibility in molecular dynamics simulations: Loading dependence of self-diffusion in carbon nanotubes. *J. Chem. Phys.* **124**, 154706 (2006).
112. Striolo, A. The mechanism of water diffusion in narrow carbon nanotubes. *Nano Lett.* **6**, 633–639 (2006).
113. Cheng, H., Cooper, A. C., Pez, G. P., Kostov, M. K., Piotrowski, P., and Stuart, S. J. Molecular dynamics simulations on the effects of diameter and chirality on hydrogen adsorption in single walled carbon nanotubes. *J. Phys. Chem. B* **109**, 3780–3786 (2005).
114. Cao, D. and Wu, J. Self-diffusion of methane in single-walled carbon nanotubes at sub- and supercritical conditions. *Langmuir* **20**, 3759–3765 (2004).
115. Arora, G., Wagner, N. J., and Sandler, S. I. Adsorption and diffusion of molecular nitrogen in single wall carbon nanotubes. *Langmuir* **20**, 6268–6277 (2004).
116. Skoulidas, A. I., Sholl, D. S., and Johnson, J. K. Adsorption and diffusion of carbon dioxide and nitrogen through single-walled carbon nanotube membranes. *J. Chem. Phys.* **124**, 054708 (2006).
117. Chen, H., Johnson, J. K., and Sholl, D. S. Transport diffusion of gases is rapid in flexible carbon nanotubes. *J. Phys. Chem. B* **110**, 1971–1975 (2006).
118. Khan, I. A. and Ayappa, K. G. Density distributions of diatoms in carbon nanotubes: A grand canonical Monte Carlo study. *J. Chem. Phys.* **109**, 4576–4586 (1998).
119. Berendsen, H. J. C., Postma, J. P. M., van Gunsteren, W. F., and Hermans, J. Interaction models for water in relation to protein hydration. In Intermolecular Forces, Pullman, B., editor, 331–342. Reidel Publishing Company, Dordrecht (1981).
120. Marti, J. and Gordillo, M. C. Temperature effects on the static and dynamic properties of liquid water inside nanotubes. *Phys. Rev. E* **64**, 021504 (2001).
121. Marti, J. and Gordillo, M. C. Time-dependent properties of liquid water isotopes adsorbed in carbon nanotubes. *J. Chem. Phys.* **114**, 10486–10492 (2001).
122. Marti, J. and Gordillo, M. C. Microscopic dynamics of confined supercritical water. *Chem. Phys. Lett.* **354**, 227–232 (2002).
123. Mashl, R. J., Joseph, S., Aluru, N. R., and Jakobsson, E. Anomalously immobilized water: A new water phase induced by confinement in nanotubes. *Nano Lett.* **3**, 589–592 (2003).
124. Koga, K., Gao, G. T., Tanaka, H., and Zeng, X. C. Formation of ordered ice nanotubes inside carbon nanotubes. *Nature* **412**, 802–805 (2001).
125. Jorgensen, W. L., Chandrasekhar, J., and Madura, J. D. Comparison of simple potential functions for simulating liquid water. *J. Chem. Phys.* **79**, 926–935 (1983).
126. Wang, J., Zhu, Y., Zhou, J., and Lu, X. H. Diameter and helicity effects on static properties of water molecules confined in carbon nanotubes. *Phys. Chem. Chem. Phys.* **6**, 829–835 (2004).
127. Noon, W. H., Ausman, K. D., Smalley, R. E., and Ma, J. Helical ice-sheets inside carbon nanotubes in the physiological condition. *Chem. Phys. Lett.* **355**, 445–448 (2002).
128. Liu, Y., Wang, Q., Wu, T., and Zhang, L. Fluid structure and transport properties of water inside carbon nanotubes. *J. Chem. Phys.* **123**, 234701 (2005).
129. Liu, Y., Wang, Q., Zhang, L., and Wu, T. Dynamics and density profile of water in nanotubes as one-dimensional fluid. *Langmuir* **21**, 12025–12030 (2005).
130. Liu, Y. and Wang, Q. Transport behavior of water confined in carbon nanotubes. *Phys. Rev. B* **72**, 085420 (2005).
131. Gordillo, M. C. and Marti, J. Hydrogen bond structure of liquid water confined in nanotubes. *Chem. Phys. Lett.* **329**, 341–345 (2000).
132. Hanasaki, I. and Nakatani, A. Hydrogen bond dynamics and microscopic structure of confined water inside carbon nanotubes. *J. Chem. Phys.* **124**, 174714 (2006).
133. Gordillo, M. C. and Marti, J. Hydrogen bonding in supercritical water confined in carbon nanotubes. *Chem. Phys. Lett.* **341**, 250–254 (2001).
134. Hummer, G., Rasaiah, J. C., and Noworyta, J. P. Water conduction through the hydrophobic channel of a carbon nanotube. *Nature* **414**, 188–190 (2001).
135. Andreev, S., Reichman, D., and Hummer, G. Effect of flexibility on hydrophobic behavior of nanotube water channels. *J. Chem. Phys.* **123**, 194502 (2005).
136. Berezhkovskii, A. and Hummer, G. Single-file transport of water molecules through a carbon nanotube. *Phys. Rev. Lett.* **89**, 064503 (2002).
137. Vaitheeswaran, S., Rasaiah, J. C., and Hummer, G. Electric field and temperature effects on water in the narrow nonpolar pores of carbon nanotubes. *J. Chem. Phys.* **121**, 7955–7965 (2004).
138. Simonyan, V. V., Johnson, J. K., Kuznetsova, A., and Jr., J. T. Y. Molecular simulation of xenon adsorption on single-walled

carbon nanotubes. *J. Chem. Phys.* **114**, 4180–4185 (2001).
139. Rols, S., Johnson, M. R., Zeppenfeld, P., Bienfait, M., Vilches, O. E., and Schneble, J. Argon adsorption in open-ended single-wall carbon nanotubes. *Phys. Rev. B* **71**, 155411 (2005).
140. Jiang, J. and Sandler, S. I. Nitrogen adsorption on carbon nanotube bundles: Role of the external surface. *Phys. Rev. B* **68**, 245412 (2003).
141. Nuzzo, R. G. and Allara, D. L. Adsorption of bifunctional organic disulfides on gold surfaces. *J. Am. Chem. Soc.* **105**, 4481–4483 (1983).
142. Ulman, A. Formation and structure of self-assembled monolayers. *Chem. Rev.* **96**, 1533–1554 (1996).
143. Love, J., Estroff, L., Kriebel, J., Nuzzo, R., and Whitesides, G. Self-assembled monolayers of thiolates on metals as a form of nanotechnology. *Chem. Rev.* **105**, 1103–1170 (2005).
144. Schreiber, F. Structure and growth of self-assembling monolayers. *Prog. Surf. Sci.* **65**, 151–256 (2000).
145. Carpick, R. W. and Salmeron, M. Scratching the surface: Fundamental investigations of tribology with atomic force microscopy. *Chem. Rev.* **97**, 1163–1194 (1997).
146. Prathima, N., Harini, M., Rai, N., Chandrashekara, R., Ayappa, K., Sampath, S., and Biswas, S. Thermal study of accumulation of conformational disorders in the self-assembled monolayers of C_8 and C_{18} alkanethiols on the Au(111) surface. *Langmuir* **21**, 2364–2374 (2005).
147. Hautman, J. and Klein, M. L. Simulation of a monolayer of alkyl thiol chains. *J. Chem. Phys.* **91**, 4994–5001 (1989).
148. Hautman, J. and Klein, M. L. Molecular dynamics simulation of the effects of temperature on a dense monolayer of long-chain molecules. *J. Chem. Phys.* **93**, 7483–7492 (1990).
149. Mar, W. and Klein, M. Molecular dynamics study of the self-assembled monolayer composed of $S(CH_2)_{14}CH_3$ molecules using an all-atoms model. *Langmuir* **10**, 188–196 (1994).
150. Ryckaert, J.-P., Ciccotti, G., and Berendsen, H. Numerical integration of the cartesian equations of motion of a system with constraints: Molecular dynamics of n-alkanes. *J. Comput. Phys.* **23**, 327 –341 (1977).
151. Ryckaert, J.-P. and Bellemans, A. Molecular dynamics of liquid alkanes. *Faraday Discussions of the Chemical Society* **66**, 95–106 (1978).
152. Bareman, J. P. and Klein, M. L. Collective tilt behavior in dense, substrate-supported monolayers of long-chain molecules: A molecular dynamics study. *J. Phys. Chem.* **94**, 5202–5205 (1990).
153. Bhatia, R. and Garrison, B. Phase transitions in a methyl-terminated monolayer self-assembled on Au(111). *Langmuir* **13**, 765–769 (1997).
154. Fenter, P., Eisenberger, P., and Liang, K. Chain-length dependence of the structures and phases of $CH_3(CH_2)_{n-1}$-SH self-assembled on Au(111). *Phys. Rev. Lett.* **70**, 2447–2450 (1993).
155. Bhatia, R. and Garrison, B. Structure of c(4×2) superlattice in alkanethiolate self-assembled monolayers. *Langmuir* **13**, 4038–4043 (1997).
156. Pertsin, A. and Grunze, M. Low-energy structures of a monolayer of octadecanethiol self-assembled on Au (111). *Langmuir* **10**, 3668–3674 (1994).
157. Gerdy, J. and Goodard, W. Atomistic structure for self-assembled monolayers of alkanethiols on Au(111) surfaces. *J. Am. Chem. Soc.* **118**, 3233–3236 (1996).
158. Siepmann, J. and McDonald, I. Domain formation and system-size dependence in simulations of self-assembled monolayers. *Langmuir* **9**, 2351–2355 (1993).
159. Siepmann, J. and McDonald, I. Monte Carlo study of the properties of self-assembled monolayers formed by adsorption of CH_3-$(CH_2)_{15}$-SH on the (111) surface of gold. *Mol. Phys.* **79**, 457–473 (1993).
160. Vemparala, S., Kalia, R., Nakano, A., and Vashishta, P. Electric field induced switching of poly(ethylene glycol) terminated self-assembled monolayers: A parallel molecular dynamics simulation. *J. Chem. Phys.* **121**, 5427–5433 (2004).
161. Rai, B., Sathish, P., Malhotra, C. P., Pradip, and Ayappa, K. G. Molecular dynamic simulations of self-assembled alkylthiolate monolayers on an Au(111) surface. *Langmuir* **20**, 3138 – 3144 (2004).
162. Luedtke, W. and Landman, U. Structure and thermodynamics of self-assembled monolayers on gold nanocrystallites. *J. Phys. Chem. B* **102**, 6566–6572 (1998).
163. Hautman, J., Bareman, J., Mar, W., and Klein, M. Molecular dynamics investigations of self-assembled monolayers. *J. Chem. Soc., Faraday Trans.* **87**, 2031–2037 (1991).
164. Röthlisberger, U., Klein, M. L., and Sprik, M. Competing interactions in self-assembled monolayers containing peptide groups: Molecular dynamics studies of long-chain perfluoro mercaptans on Au(111). *J. Mater. Chem.* **4**, 793–803 (1994).
165. Jung, H., Won, Y., Shin, S., and Kim, K. Molecular dynamics simulation of benzenethiolate and benzyl mercaptide on Au(111). *Langmuir* **15**, 1147–1154 (1999).
166. Osman, M., Ernst, M., Meier, B., and Suter, U. Structure and molecular dynamics of alkane monolayers self-assembled on mica platelets. *J. Phys. Chem. B* **106**, 653–662 (2002).
167. Heinz, H., Castelijns, H. J., and Suter, U. W. Structure and phase transition of alkyl chains on mica. *J. Am. Chem. Soc.* **125**, 9500–9510 (2003).
168. Jang, Y., Jang, S., and Goddard, W. Molecular dynamics simulation study on a monolayer of half [2]rotaxane self-assembled on Au(111). *J. Am. Chem. Soc.* **127**, 4959–4964 (2005).
169. Duffy, D. M. and Harding, J. H. Modeling the properties of self-assembled monolayers terminated by carboxylic acids. *Langmuir* **21**, 3850–3857 (2005).
170. Zheng, J., He, Y., Chen, S., Li, L., Bernards, M., and Jiang, S. Molecular simulation studies of the structure of phosphorylcholine self-assembled monolayers. *J. Chem. Phys.* **125**, 174714 (2006).
171. Siepmann, J. and McDonald, I. Monte Carlo simulations of mixed monolayers. *Mol. Phys.* **75**, 255–259 (1992).
172. Jiang, S. Molecular simulation studies of self-assembled monolayers of alkanethiols on Au(111). *Mol. Phys.* **100**, 2261–2275 (2002).
173. Hung, S.-W., Hwang, J.-K., Tseng, F., Chang, J., Chen, C.-C., and Chieng, C. Molecular dynamics simulation of the enhancement of cobra cardiotoxin and E6 protein binding on mixed self-assembled monolayer molecules. *Nanotechnology* **17**, S8 (2006).
174. Siepmann, J. and McDonald, I. Monte Carlo simulation of the mechanical relaxation of a self-assembled monolayer. *Phys. Rev. Lett.* **70**, 453–456 (1993).
175. Joyce, S. A., Thomas, R. C., Houston, J. E., Michalske, T. A., and Crooks, R. M. Mechanical relaxation of organic monolayer films measured by force microscopy. *Phys. Rev. Lett.* **68**, 2790–2793 (1992).
176. Tupper, K., Colton, R., and Brenner, D. Simulations of self-assembled monolayers under compression: Effect of surface asperities. *Langmuir* **10**, 2041–2043 (1994).
177. Tupper, K. and Brenner, D. Compression-induced structural transition in a self-assembled monolayer. *Langmuir* **10**, 2335–2338 (1994).
178. Bonner, T. and Baratoff, A. Molecular dynamics study of scanning force microscopy on self-assembled monolayers. *Surf. Sci.* **377-379**, 1082–1086 (1997).
179. Tutein, A. B., Stuart, S. J., and Harrison, J. A. Role of defects in compression and friction of anchored hydrocarbon chains on diamond. *Langmuir* **16**, 291–296 (2000).
180. Mikulski, P. and Harrison, J. Packing-density effects on the friction of n-alkane monolayers. *J. Am. Chem. Soc.* **123**, 6873–6881 (2001).

181. Mikulski, P. T., Herman, L. A., and Harrison, J. A. Odd and even model self-assembled monolayers: Links between friction and structure. *Langmuir* **21**, 12197–12206 (2005).
182. Chandross, M., Grest, G. S., and Stevens, M. J. Friction between alkylsilane monolayers: Molecular simulation of ordered monolayers. *Langmuir* **18**, 8392–8399 (2002).
183. Park, B., M., C., Stevens, M., and Grest, G. Chemical effects on the adhesion and friction between alkanethiol monolayers: Molecular dynamics simulations. *Langmuir* **19**, 9239–9245 (2003).
184. B., P., Christian, D. L., Michael, C. Mark, J. S., and Gary, S. G. Frictional dynamics of flourine - terminated alkane thiol self-assembled monolayers. *Langmuir* **20**, 10007–10014 (2004).
185. Chandross, M., Webb III, E., Stevens, M., Grest, G., and Garofalini, S. Systematic study of the effect of disorder on nanotribology of self-assembled monolayers. *Phys. Rev. Lett.* **93**, 166103 (2004).
186. Zhang, L., Goddard, W., and Jiang, S. Molecular simulation study of the c(4×2) superlattice structure of alkanethiol self-assembled monolayers on Au(111). *J. Chem. Phys.* **117**, 7342–7349 (2002).
187. Zhang, L. and Jiang, S. Molecular simulation study of nanoscale friction between alkyl monolayers on Si(111) immersed in solvents. *J. Chem. Phys.* **119**, 765–770 (2003).
188. Leng, Y. and Jiang, S. Atomic indentation and friction of self-assembled monolayers by hybrid molecular simulations. *J. Chem. Phys* **113**, 8800 –8806 (2000).
189. Leng, Y. and Jiang, S. Dissipative process in atomic force microscopy. *Phys. Rev. B* **64**, 115415 (2001).
190. Leng, Y. and Jiang, S. Dynamic simulation of adhesion and friction in chemical force microscopy. *J. Am. Chem. Soc.* **124**, 11764–11770 (2002).
191. Patrick, D., Flanagan, J., Kohl, P., and Lynden-Bell, R. Atomistic molecular dynamics simulations of chemical force microscopy. *J. Am. Chem. Soc.* **125**, 6762–6773 (2003).
192. Sung, I.-H. and Kim, D.-E. Molecular dynamics simulation study of the nano-wear characteristics of alkanethiol self-assembled monolayers. *Appl. Phys. A* **81**, 109–114 (2005).
193. Shiokawa, T., Ohzono, T., and Fujihira, M. Molecular dynamics simulation of non-contact atomic force microscopy of an ordered monolayer consisting of single united atoms chemisorbed strongly on a continuum substrate. *Appl. Surf. Sci.* **210**, 117–122 (2003).
194. Bat-Uul, B., Fujii, S., Shiokawa, T., Ohzono, T., and Fujihira, M. Molecular dynamics simulation of non-contact atomic force microscopy of self-assembled monolayers on Au (111). *Nanotechnology* **15**, 710–715 (2004).
195. Kranenburg, M., Venturoli, M., and Smit, B. Phase behavior and induced interdigitation in bilayers studied with dissipative particle dynamics. *J. Phys. Chem. B* **107**, 11491–11501 (2003).
196. Hoogerbrugge, P. J. and Koelman, J. M. V. A. Simulating microscopic hydrodynamic phenomena with dissipative particle dynamics. *Europhys. Lett.* **19**, 155–160 (1992).
197. Koelman, J. and Hoogerbrugge, P. Dynamic simulations of hard sphere suspensions under steady shear. *Europhys. Lett.* **21**, 363–368 (1993).
198. Español, P. and Warren, P. Statistical mechanics of dissipative particle dynamics. *Europhys. Lett.* **30**, 191–196 (1995).
199. Groot, R. D. and Warren, P. B. Dissipative particle dynamics: Bridging the gap between atomistic and mesoscopic simulation. *J. Chem. Phys.* **107**, 4423–4435 (1997).
200. Venturoli, M., Smit, B., and Sperotto, M. M. Simulation studies of protein-induced bilayer deformations, and lipid-induced protein tilting, on a mesoscopic model for lipid bilayers with embedded proteins. *Biophys. J.* **88**, 1778–1798 (2005).
201. Keaveny, E. E., Pivkin, I. V., Maxey, M., and Karniadakis, G. E. A comparative study between dissipative particle dynamics and molecular dynamics for simple- and complex-geometry flows. *J. Chem. Phys* **123**, 104107 (2005).
202. Maiti, A. and McGrother, S. Bead–bead interaction parameters in dissipative particle dynamics: Relation to bead-size, solubility parameter, and surface tension. *J. Chem. Phys* **120**, 1594–1601 (2004).
203. Vattulainen, I., Karttunen, M., Besold, G., and Polson, J. M. Integration schemes for dissipative particle dynamics simulations: From softly interacting systems towards hybrid models. *J. Chem. Phys* **116**, 3967–3979 (2002).
204. Nikunen, P., Karttunen, M., and Vattulainen, I. How would you integrate equations of motion in dissipative particle dynamics simulations? *Computer Physics Communications* **153**, 407–423 (2003).
205. Hafskjold, B., Liew, C. C., and Shinoda, W. Can such long time steps really be used in dissipative particle dynamics simulations? *Molecular Simulation* **30**, 879–885 (2004).
206. Allen, M. Configurational temperature in membrane simulations using dissipative particle dynamics. *J. Phys. Chem. B* **110**, 3823–3830 (2006).
207. Groot, R. D. and Rabone, K. L. Mesoscopic simulation of cell membrane damage, morphology change and rupture by nonionic surfactants. *Biophys. J.* **81**, 725–736 (2001).
208. Lyubartsev, A., Karttunen, M., Vattulainen, I., and Laaksonen, A. On coarse-graining by the inverse Monte Carlo method: Dissipative particle dynamics simulations made to a precise tool in soft matter modeling. *Soft Materials* **1**, 121 (2002).
209. Lees, A. W. and Edwards, S. F. The computer study of transport processes under extreme conditions. *J. Phys. C* **5**, 1921–1928 (1972).
210. Willemsen, S., Hoefsloot, H., and Iedema, P. No-slip boundary condition in dissipative particle dynamics. *Int. J. Mod. Phys. C* **11**, 881 (2000).
211. Fan, X., Phan-Thien, N., Yong, N. T., Wu, X., and Xu, D. Microchannel flow of a macromolecular suspension. *Physics of Fluids* **15**, 11–21 (2003).
212. Liu, M., Meakin, P., and Huang, H. Dissipative particle dynamics with attractive and repulsive particle-particle interactions. *Physics of Fluids* **18**, 017101 (2006).
213. Chen, S., Phan-Thien, N., Khoo, B. C., and Fan, X. J. Flow around spheres by dissipative particle dynamics. *Physics of Fluids* **18**, 103605 (2006).
214. Boek, E. S., Coveney, P. V., Lekkerkerker, H. N. W., and van der Schoot, P. Simulating the rheology of dense colloidal suspensions using dissipative particle dynamics. *Phys. Rev. E* **55**, 3124–3133 (1997).
215. Pryamitsyn, V. and Ganesan, V. A coarse-grained explicit solvent simulation of rheology of colloidal suspensions. *J. Chem. Phys* **122**, 104906 (2005).
216. Español, P. Fluid particle dynamics: A synthesis of dissipative particle dynamics and smoothed particle dynamics. *Europhys. Lett.* **39**, 605–610 (1997).
217. Dzwinel, W. and Yuen, D. Matching macroscopic properties of binary fluids to the interactions of dissipative particle dynamics. *Int. J. Mod. Phys. C* **11**, 1 (2000).
218. Tiwari, A. and Abraham, J. Dissipative-particle-dynamics model for two-phase flows. *Phys. Rev. E* **74**, 056701 (2006).
219. Revenga, M., Zúñiga, I., and Español, P. Boundary conditions in dissipative particle dynamics. *Computer physics communications* **121-122**, 309–311 (1999).
220. Pivkin, I. V. and Karniadakis, G. E. Controlling density fluctuations in wall-bounded dissipative particle dynamics systems. *Phys. Rev. Lett.* **96**, 206001 (2006).
221. Schlijper, A. G., Hoogerbrugge, P. J., and Manke, C. W. Computer simulation of dilute polymer solutions with the dissipative particle dynamics method. *J. Rheol.* **39**, 567–579 (1995).
222. Kong, Y., Manke, C. W., Madden, W. G., and Schlijper, A. G. Effect of solvent quality on the conformation and relaxation

of polymers via dissipative particle dynamics. *J. Chem. Phys* **107**, 592–602 (1997).
223. Symeonidis, V., Karniadakis, G. E., and Caswell, B. Dissipative particle dynamics simulations of polymer chains: Scaling laws and shearing response compared to DNA experiments. *Phys. Rev. Lett.* **95**, 076001 (2005).
224. Pan, G. and Manke, C. W. Effects of solvent quality on the dynamics of polymer solutions simulated by dissipative particle dynamics. *J. Rheol.* **46**, 1221–1237 (2002).
225. Qian, H.-J., Lu, Z.-Y., Chen, L.-J., Li, Z.-S., and Sun, C.-C. Dissipative particle dynamics study on the interfaces in incompatible A/B homopolymer blends and with their block copolymers. *J. Chem. Phys* **122**, 184907 (2005).
226. Groot, R. D. and Madden, T. J. Dynamic simulation of diblock copolymer microphase separation. *J. Chem. Phys* **108**, 8713–8724 (1998).
227. Jury, S., Bladon, P., Cates, M., Krishna, S., Hagen, M., Ruddok, N., and Warren, P. Simulation of amphiphilic mesophases using dissipative particle dynamics. *Phys. Chem. Chem. Phys.* **1**, 2051–2056 (1999).
228. Nakamura, H. and Tamura, Y. Phase diagram for self-assembly of amphiphilic molecule $C_{12}E_6$ by dissipative particle dynamics. *Computer Physics Communications* **169**, 139–143 (2005).
229. Kranenburg, M. and Smit, B. Simulating the effect of alcohol on the structure of a membrane. *FEBS Lett.* **568**, 15–18 (2004).
230. Kranenburg, M. and Smit, B. Phase behavior of model lipid bilayers. *J. Phys. Chem. B* **109**, 6553–6563 (2005).
231. Shillcock, J. C. and Lipowsky, R. Equilibrium structure and lateral stress distribution of amphiphilic bilayers from dissipative particle dynamics simulations. *J. Chem. Phys* **117**, 5048–5061 (2002).
232. Illya, G., Lipowsky, R., and Shillcock, J. C. Effect of chain length and asymmetry on material properties of bilayer membranes. *J. Chem. Phys* **122**, 244901 (2005).
233. Li, D.-W., Liu, X. Y., and Feng, Y. P. Bond-angle-potential-dependent dissipative particle dynamics simulation and lipid inverted phase. *J. Phys. Chem. B* **108**, 11206–11213 (2004).
234. Yamamoto, S., Maruyama, Y., and aki Hyodo, S. Dissipative particle dynamics study of spontaneous vesicle formation of amphiphilic molecules. *J. Chem. Phys* **116**, 5842–5849 (2002).
235. Yamamoto, S., Maruyama, Y., and aki Hyodo, S. Erratum: Dissipative particle dynamics study of spontaneous vesicle formation of amphiphilic molecules. *J. Chem. Phys* **117**, 2990–2990 (2002).
236. Laradji, M. and Kumar, P. B. S. Domain growth, budding, and fission in phase-separating self-assembled fluid bilayers. *J. Chem. Phys.* **123**, 224902 (2005).
237. Li, D.-W. and Liu, X. Y. Examination of membrane fusion by dissipative particle dynamics simulation and comparison with continuum elastic models. *J. Chem. Phys* **122**, 174909 (2005).
238. Español, P. Statistical mechanics of coarse graining. *Lecture Notes in Physics, Springer-Verlag: Berlin.* **640** (2004).
239. Nielsen, S. O., Lopez, C. F., Srinivas, G., and Klein, M. L. Coarse grain models and the computer simulation of soft materials. *J. Phys.: Condens. Matter* **16**, R481–R512 (2004).

Ateeque Malani is a PhD student of Department of Chemical Engineering at Indian Institute of Science (IISc) working with Prof. K. G. Ayappa. He has done his Masters(Chemical Engineering) from Indian Institute of Technology(IIT), Bombay in 2004, and Bachelors (Chemical Engineering) from Jawaharlal Darda Institute of Engineering and Technology (JDIET) in 2002. His research involves understanding structure and dynamics of water and electrolytes confined in nanopores using molecular simulation techniques.

Foram Thakkar is a Ph.D. student at Department of Chemical engineering at Indian Institute of Science(IISc) working with Prof. K. G. Ayappa His area of research includes the study of complex fluids using mesoscale simulation techniques such as dissipative particle dynamics. He has done his M. Tech in chemical engineering from Indian Instititute of Technology, Kharagpur in 2004. He has completed his B. E. in chemical engineering from Gujarat University, Ahmedabad in 2002.

Patil kalyan is a Ph.D. student at Department of Chemical engineering at Indian Institute of Science working jointly with Prof. K. G. Ayappa and Prof. S. K. Biswas (Mechanical Engineering). His area of research includes characterizing surfaces modified with self-assembled monolayers using atomic force microscopy. He has done his masters in chemical engineering from Birla institute of Science and Technology (BITS), Pilani in 2003. He has completed his bachelor of technology program in petrochemical engineering from Dr. Babasaheb Ambedkar technological university, Lonere in 2000.

K. G. Ayappa is Professor in the Department of Chemical Engineering Indian Institute of Science, Bangalore. His research interests lie in probing the structure and dynamics of fluids confined in nanopores, complex fluid interfaces and phase transitions using statistical mechanics and molecular simulation techniques. Prof Ayappa recevied his BE degree from Mangalore University in 1984, MS (1987) and PhD (1992) from the University of Minnesota.